Article

A brain-to-gut signal controls intestinal fat absorption

https://doi.org/10.1038/s41586-024-07929-5

Received: 28 January 2022

Accepted: 8 August 2024

Published online: 11 September 2024

Check for updates

Qianqian Lyu[1,2,9], Wenzhi Xue[1,3,9], Ruixin Liu[1,2,9], Qinyun Ma[1,2,9], Vikram Babu Kasaragod[4,9], Shan Sun[5,9], Qian Li[1], Yanru Chen[1], Mingyang Yuan[1], Yuying Yang[1], Bing Zhang[5], Aifang Nie[1,2], Sheng Jia[1], Chongrong Shen[1], Po Gao[6], Weifang Rong[6], Chenxi Yu[7], Yufang Bi[1,2], Chunlei Zhang[8], Fajun Nan[7], Guang Ning[1,2], Zihe Rao[5], Xiuna Yang[5], Jiqiu Wang[1,2]✉ & Weiqing Wang[1,2]✉

Although fat is a crucial source of energy in diets, excessive intake leads to obesity. Fat absorption in the gut is prevailingly thought to occur organ-autonomously by diffusion[1–3]. Whether the process is controlled by the brain-to-gut axis, however, remains largely unknown. Here we demonstrate that the dorsal motor nucleus of vagus (DMV) plays a key part in this process. Inactivation of DMV neurons reduces intestinal fat absorption and consequently causes weight loss, whereas activation of the DMV increases fat absorption and weight gain. Notably, the inactivation of a subpopulation of DMV neurons that project to the jejunum shortens the length of microvilli, thereby reducing fat absorption. Moreover, we identify a natural compound, puerarin, that mimics the suppression of the DMV–vagus pathway, which in turn leads to reduced fat absorption. Photoaffinity chemical methods and cryogenic electron microscopy of the structure of a $GABA_A$ receptor–puerarin complex reveal that puerarin binds to an allosteric modulatory site. Notably, conditional *Gabra1* knockout in the DMV largely abolishes puerarin-induced intestinal fat loss. In summary, we discover that suppression of the DMV–vagus–jejunum axis controls intestinal fat absorption by shortening the length of microvilli and illustrate the therapeutic potential of puerarin binding to GABRA1 in fat loss.

The predominant increase in fat and calorie-dense food consumption worldwide has contributed substantially to the ongoing pandemic of obesity and metabolic disorders[4]. To take up fat effectively, the animal intestine has evolved into an absorption system comprising a long intestine with a protruding villus structure, brush-border microvilli and abundant enteric vascular and lymph vessels and nerve terminals[5–7]. The system is finely tuned to respond to fluctuations in the energy supply status, including the fasting-to-refeeding transition and a switch from a low-fat diet to a high-fat diet (HFD)[8]. Of note, intestinal fat absorption has been commonly recognized as an organ-autonomous process, mainly in the form of diffusion and partially through protein-facilitated lipid transport[1–3]. Recent observations have indicated a potential link between brain-derived factors and fat absorption in the small intestine. For instance, ablation of leptin receptors in hypothalamic neurons is reported to disrupt the expression of intestinal microsomal triglyceride transfer proteins[9].

In the vagus nerve system, the nucleus tractus solitarius (NTS) and the DMV act as the hub of the brain–gut axis[10]. After the NTS receives multiple vagal afferent inputs from the intestine and integrates them with inputs from other areas[11], the combined signals are relayed to the DMV, in which distinct neurons provide different output responses to regulate gastrointestinal motility and enhance digestion[12]. Vagotomy together with antrectomy leads to reduced fat absorption through impaired gastric motility, with poor digestion of food particles in the intestine[13]. Whether vagal efferent nerves from the DMV physiologically and directly regulate intestinal fat absorption is unclear.

In this study, we manipulated the activity of DMV neurons to reveal their roles in controlling jejunal fat absorption. We show that administration of puerarin, a drug used for treating cerebrovascular diseases[14], enhances faecal fat excretion and weight loss through the inhibition of $GABA_A$ receptor α1 subunit (GABRA1)-positive DMV neurons. These findings demonstrate a previously unknown brain-to-gut axis that controls intestinal fat absorption and identify an applicable drug, puerarin, that targets this pathway.

The DMV regulates jejunal fat absorption

Given the central role of the DMV in the brain-to-gut pathway[10], we first evaluated the effects of DMV neuronal inactivation on intestinal fat absorption. We used the chemogenetic designer receptor

[1]Department of Endocrine and Metabolic Diseases, Shanghai Institute of Endocrine and Metabolic Diseases, Ruijin Hospital, Shanghai Jiao Tong University School of Medicine (SJTUSM), Shanghai, China. [2]Shanghai National Clinical Research Center for Metabolic Diseases, Key Laboratory for Endocrine and Metabolic Diseases of the National Health Commission of the PR China, Shanghai National Center for Translational Medicine, Ruijin Hospital, SJTUSM, Shanghai, China. [3]Clinical Neuroscience Center, Ruijin Hospital Luwan Branch, SJTUSM, Shanghai, China. [4]MRC Laboratory of Molecular Biology, Cambridge, UK. [5]Shanghai Institute for Advanced Immunochemical Studies, ShanghaiTech University, Shanghai, China. [6]Department of Anatomy and Physiology, SJTUSM, Shanghai, China. [7]The Chinese National Center for Drug Screening, Shanghai Institute of Materia Medica, Chinese Academy of Sciences, Shanghai, China. [8]Institut Pasteur, Université de Paris, Neural Circuits for Spatial Navigation and Memory, Paris, France. [9]These authors contributed equally: Qianqian Lyu, Wenzhi Xue, Ruixin Liu, Qinyun Ma, Vikram Babu Kasaragod, Shan Sun. ✉e-mail: wangjq@shsmu.edu.cn; wqingw@shsmu.edu.cn

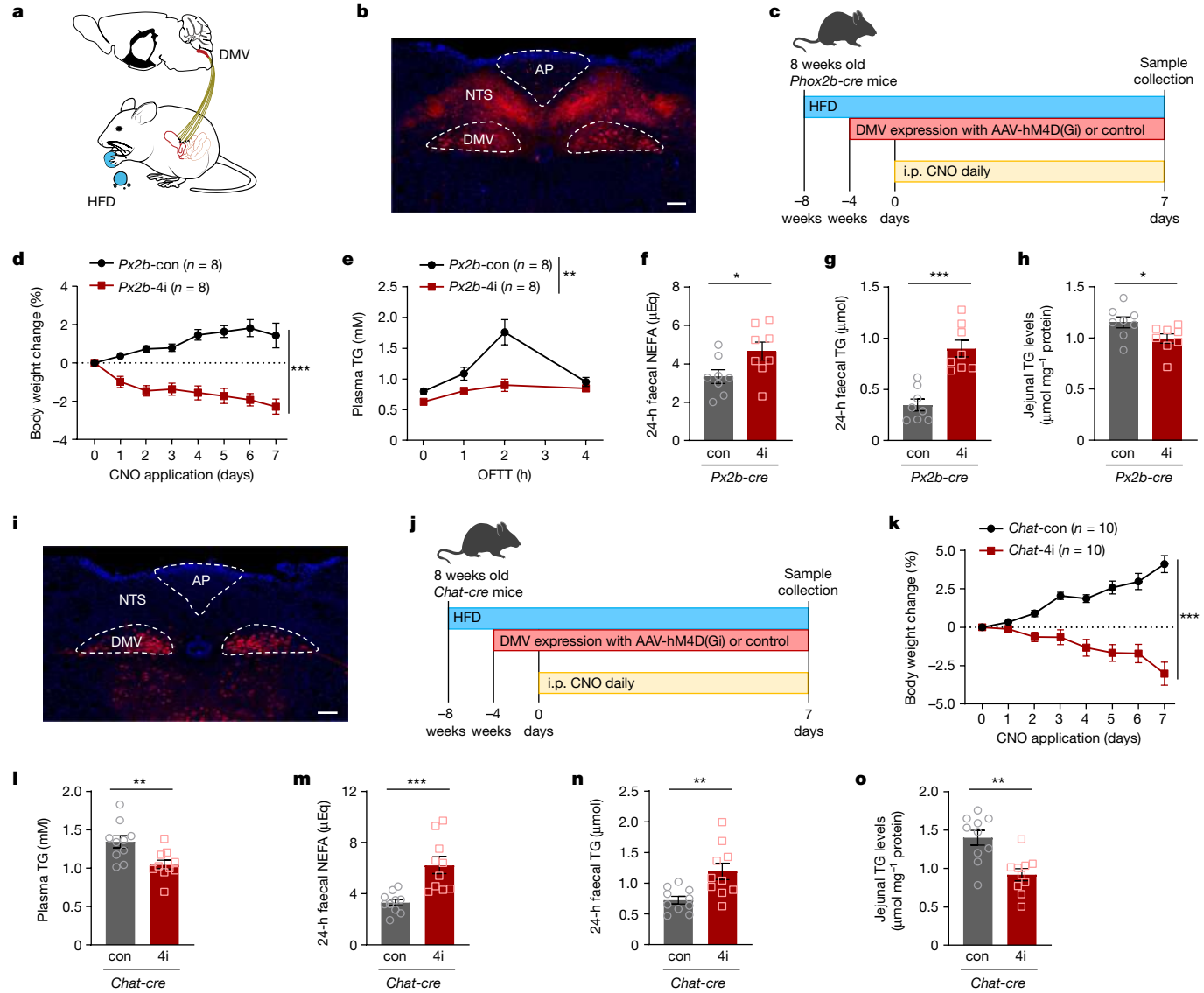

Fig. 1 | The DMV controls jejunal fat absorption and body weight gain. **a**, Abridged view of the brainstem–vagus nerve–intestine pathway in mice fed a HFD. **b**, PHOX2B-positive neurons in the brainstem of PHOX2B-Cre:Rosa26-tdTomato mice. AP, area postrema. **c**, Schematic of the experimental design using chemogenetic suppression of DMV activity in *Phox2b-cre* mice. **d**–**h**, Changes observed after inactivation of DMV neurons in *Px2b*-4i mice and *Px2b*-con mice ($n = 8$ per group). Body weight change (**d**), plasma TG levels after OFTTs (**e**), 24-h faecal NEFA (**f**) and TG content (**g**), and jejunal TG levels (**h**). **i**, CHAT-positive neurons located in the DMV of CHAT-Cre:Rosa26-tdTomato mice. **j**, Schematic of the experimental design using chemogenetic suppression of DMV function in *Chat-cre* mice. **k**–**o**, Changes observed after inactivation of DMV neurons in *Chat*-4i mice ($n = 10$ per group). Body weight change (**k**), plasma TG levels (**l**), 24-h faecal NEFA (**m**) and TG content (**n**), and jejunal TG levels (**o**). Sample collection was at day 7 after CNO application. Plasma and jejunal samples were collected 2 h after 200 μl olive oil gavage. Scale bar, 100 μm (**b**,**i**). Data presented as the mean ± s.e.m. Significance was assessed using two-way analysis of variance (ANOVA) (**d**,**e**,**k**), two-tailed Student's *t*-test (**f**,**g**,**l**–**o**) or two-tailed Mann–Whitney test (**h**). $^*P < 0.05$, $^{**}P < 0.01$, $^{***}P < 0.001$. For detailed statistics, see source data. The mouse model in **a** was adapted from SciDraw (https://scidraw.io) under a Creative Commons licence CC BY-SA 4.0.

exclusively activated by designer drugs (DREADDS) technique[15] and bilaterally injected recombinant adeno-associated virus (rAAV) expressing Cre-dependent hM4D(Gi) (rAAV-EF1α-DIO-hM4D(Gi)-mCherry)[16] or control AAV (rAAV-EFLA-DIO-mCherry) into the DMV region of *Phox2b-cre* heterozygous mice. This approach enabled us to specifically target a population of PHOX2B neurons in the DMV[17] (Fig. 1a–c). Clozapine *N*-oxide (CNO), a ligand of the chemogenetic designer receptor, was shown to inactivate DMV neurons ex vivo (Extended Data Fig. 1a–c). After intraperitoneal (i.p.) CNO injection, mice in which DMV neurons were inhibited (*Px2b*-4i) fed on a HFD showed less body weight gain than control mice (*Px2b*-con) (Fig. 1d and Supplementary Fig. 1a) with no difference in food consumption (Supplementary Fig. 1b). An oral fat tolerance test (OFTT) was conducted to compare intestinal triglyceride (TG) absorption between the groups. *Px2b*-4i mice showed lower plasma TG levels than *Px2b*-con mice after oil gavage (Fig. 1e). Faeces collected from *Px2b*-4i mice had significantly higher contents of non-esterified fatty acid (NEFA) and TG (Fig. 1f,g) than faeces from control mice, which indicated an increase in fat excretion after DMV inhibition. Consistently, we observed decreased fat absorption in the jejunum of *Px2b*-4i mice (Fig. 1h), the main site responsible for lipid absorption[18,19]. We also performed an oral glucose tolerance test and observed no significant difference in blood glucose levels between groups (Supplementary Fig. 1c). These findings suggest that DMV inhibition leads to a reduction in jejunal fat absorption.

To confirm that the above intestinal phenotypes primarily resulted from the inactivation of DMV neurons rather than other

Phox2b-expressing neurons, such as those in the NTS, we further performed chemogenetic inactivation of DMV neurons in *Chat-cre* mice. In these mice, Cre recombinase is selectively expressed in cholinergic ($CHAT^+$) neurons, which are primarily located in the DMV but not in the NTS[20,21] (Fig. 1i). We injected Cre-dependent AAV-hM4D(Gi) into the DMV of *Chat-cre* mice (Fig. 1j). After CNO application, we observed significant changes in *Chat*-4i mice, such as less body weight gain, lower plasma TG levels, more faecal fat excretion and less jejunal fat absorption compared with *Chat*-con mice (Fig. 1k–o and Supplementary Fig. 1d,e). These results were consistent with the phenotypes in *Px2b*-4i mice and validated the suppressive effects of DMV inhibition on jejunal fat absorption.

Next, we activated DMV neurons with a bilateral injection of hM3D(Gq) (rAAV-EF1α-DIO-hM3D(Gq)-mCherry) into the DMV of *Phox2b-cre* mice (3q) (Extended Data Fig. 1d–f). We also designated two other groups of *Phox2b-cre* mice as controls, which were injected with either hM4D(Gi) (4i) or control virus (con) (Extended Data Fig. 2a). After CNO-induced activation of DMV neurons, we observed enhanced body weight gain (Extended Data Fig. 2b,c), reduced faecal NEFA and TG excretion (Extended Data Fig. 2d,e) and increased jejunal TG content (Extended Data Fig. 2f) compared with *Px2b*-con mice. Results from long-term activation of DMV neurons in *Px2b*-3q mice showed the opposite effects when compared with *Px2b*-4i mice (Extended Data Fig. 2b–f). Of note, we did not find significant changes in the TG content in other intestinal segments, such as the duodenum or the ileum after DMV manipulation (Extended Data Fig. 2g,h).

To confirm the role of the DMV–vagus pathway in intestinal fat absorption, we performed subdiaphragmatic vagotomy (Extended Data Fig. 3a). Vagotomy resulted in less body weight gain (Extended Data Fig. 3b), increased fat excretion (Extended Data Fig. 3c,d) and reduced jejunal fat absorption (Extended Data Fig. 3e). Together, these findings demonstrate that the activity of the DMV has a key role in regulating jejunal fat absorption and consequently causing body weight change.

Identification of puerarin for DMV suppression

To identify chemical molecules or natural compounds that regulate DMV neurons, we utilized a combination of pharmacological treatments with electrophysiology of brainstem slices prepared from PHOX2B-Cre:Rosa26-tdTomato mice. Bath application of puerarin (Extended Data Fig. 4a), an approved drug for treating cardiocerebrovascular diseases[22], induced a significant reduction in the action potential frequency (Fig. 2a,b), which was due to membrane potential hyperpolarization in DMV neurons (Fig. 2c). Among a total of 22 detected neurons, 16 (72.7%) showed a puerarin-inhibited pattern of firing change (Fig. 2d). In mice fed a HFD after i.p. injection of puerarin, the number of FOS-positive neurons in the DMV was significantly reduced compared with control mice (Fig. 2e,f and Extended Data Fig. 4b–j). We also observed that puerarin (i.p.) treatment reduced body weight gain without affecting food intake (Fig. 2g,h and Supplementary Fig. 2a,b), decreased plasma TG levels (based on the OFTT; Fig. 2i), increased faecal fat excretion (Fig. 2j,k) and suppressed jejunal fat absorption (Fig. 2l). In line with the results of DMV inhibition, puerarin treatment did not significantly affect oral glucose tolerance (Supplementary Fig. 2c) or the TG content in the duodenum and the ileum (Supplementary Fig. 2d,e). Moreover, gastrointestinal motility and transit were not affected by puerarin (Supplementary Fig. 2f–o). To avoid potential confounding effects of puerarin on peripheral organs, pair-fed HFD mice were given an intracerebroventricular (i.c.v) infusion of puerarin into the lateral ventricle (Fig. 2m). Puerarin treatment consistently suppressed body weight gain and reduced plasma TG levels (Fig. 2n,o and Supplementary Fig. 2p). Notably, we also observed that central administration of puerarin increased total faecal lipid content (Fig. 2p,q) and reduced jejunal TG content (Fig. 2r). Together, these results demonstrate that puerarin has an inhibitory role in controlling DMV activity, which leads to a reduction in jejunal fat absorption.

Puerarin targets GABRA1 to suppress the DMV

To elucidate the molecular mechanism that mediates the suppressive effect of DMV neurons on fat absorption, we next performed an activity-based protein profiling strategy[23] using puerarin as the bait. The puerarin-tag probe was synthesized with a photoreactive tag (Extended Data Fig. 5a) to enrich and visualize target proteins through a photoaffinity chemistry reaction[24] (Fig. 3a). We verified that probe-tagged puerarin retains the same effects of increasing faecal lipid excretion as non-tagged puerarin (Extended Data Fig. 5b–f). Probe-tagged puerarin was added to freshly isolated brainstem samples, and ten doses of non-tagged puerarin was used as a competitor of probe-tagged puerarin (Methods). Following the photoaffinity reaction, targeted proteins were subsequently assessed by liquid chromatography and tandem mass spectrometry (LC–MS/MS). Of the 571 potential target proteins (Fig. 3b and Supplementary Table 1), only 14 candidates were attributed to membrane receptors and ion channels. Among these 14 proteins, GABRA1 was prioritized as a promising target given that it is abundantly expressed in the DMV and less expressed in adjacent brain regions (Allen Brain Map database)[25] (Extended Data Fig. 5g). Moreover, the $GABA_A$ receptor has been implicated in vagal modulation[26]. We validated the interactions between probe-tagged puerarin and GABRA1 protein by western blotting (Fig. 3c and Supplementary Fig. 3). We also detected that probe-tagged puerarin highly colocalized with GABRA1 in PHOX2B-tdTomato neurons in the DMV region, and these signals could be blocked by ten doses of non-tagged puerarin (Fig. 3d).

$GABA_A$ receptors are pentameric ligand-gated ion channels and the principal determinants of inhibitory neurotransmission in the vertebrate nervous system[27]. To characterize the effect of puerarin on α1-subunit-containing $GABA_A$ receptors, we used the α1β3γ2L heteropentamer, a prototypical neuronal subtype[28]. First, through whole-cell patch-clamp recording of HEK293S cells expressing this receptor, we found that puerarin amplified the GABA-induced current (Fig. 3e,f and Extended Data Fig. 6a). We next solved a single-particle cryogenic electron microscopy (cryo-EM) structure of α1β3γ2L $GABA_A$ receptor bound to puerarin to a nominal resolution of 2.4 Å (Fig. 3g, Extended Data Fig. 6b,c and Extended Data Table 1). Puerarin density was observed in a single location, under loop C at the $\alpha1^+/\gamma2^-$ interface (Fig. 3g and Extended Data Fig. 6d–f), a classical binding site for benzodiazepines and other allosteric modulators in the extracellular region of synaptic $GABA_A$ receptors[29–31]. In this pocket, puerarin covers a surface area of 587 $Å^2$. Its hydroxyphenyl group points towards the γ2-C^- subunit, and the chromone and glucoside groups contact mainly the α1-D^+-subunit. The α1Tyr210 and γ2Phe77 residues anchor the puerarin chromone core through π–π stacking interactions. In addition to water-mediated contacts, puerarin binding is stabilized by a hydrogen-bonding network that involves the loop C residues α1Ser205 and α1Thr207, as well as α1His102 and γ2Asp56 (Fig. 3h and Extended Data Fig. 6d–f). Alongside the agonist GABA, bound to the orthosteric sites at the two $\beta3^+/\alpha1^-$ interfaces (Extended Data Fig. 6g), puerarin binding drives the ion channel into a deep desensitized state as revealed by the relative domain arrangements and 9′-activation gate, which is wider than in the previously reported diazepam-bound structures[29] (Extended Data Fig. 6h–j). These structural data, together with the electrophysiological recordings, demonstrate that puerarin acts as a positive allosteric modulator.

To confirm that puerarin can suppress fat absorption through DMV GABRA1, we crossed *Gabra1*$^{flox/flox}$ (*Gabra1*$^{fl/fl}$) mice with *Phox2b-cre* mice to generate *Gabra1* conditional knockout (cKO) mice (Extended Data Fig. 7a). In the absence of *Gabra1* (Extended Data Fig. 7b), we observed increased DMV neuronal activity (Extended Data Fig. 7c–e), increased body weight gain (Fig. 3i,j and Extended Data Fig. 7g), reduced faecal fat excretion (Fig. 3k,l) and increased jejunal fat absorption (Fig. 3m)

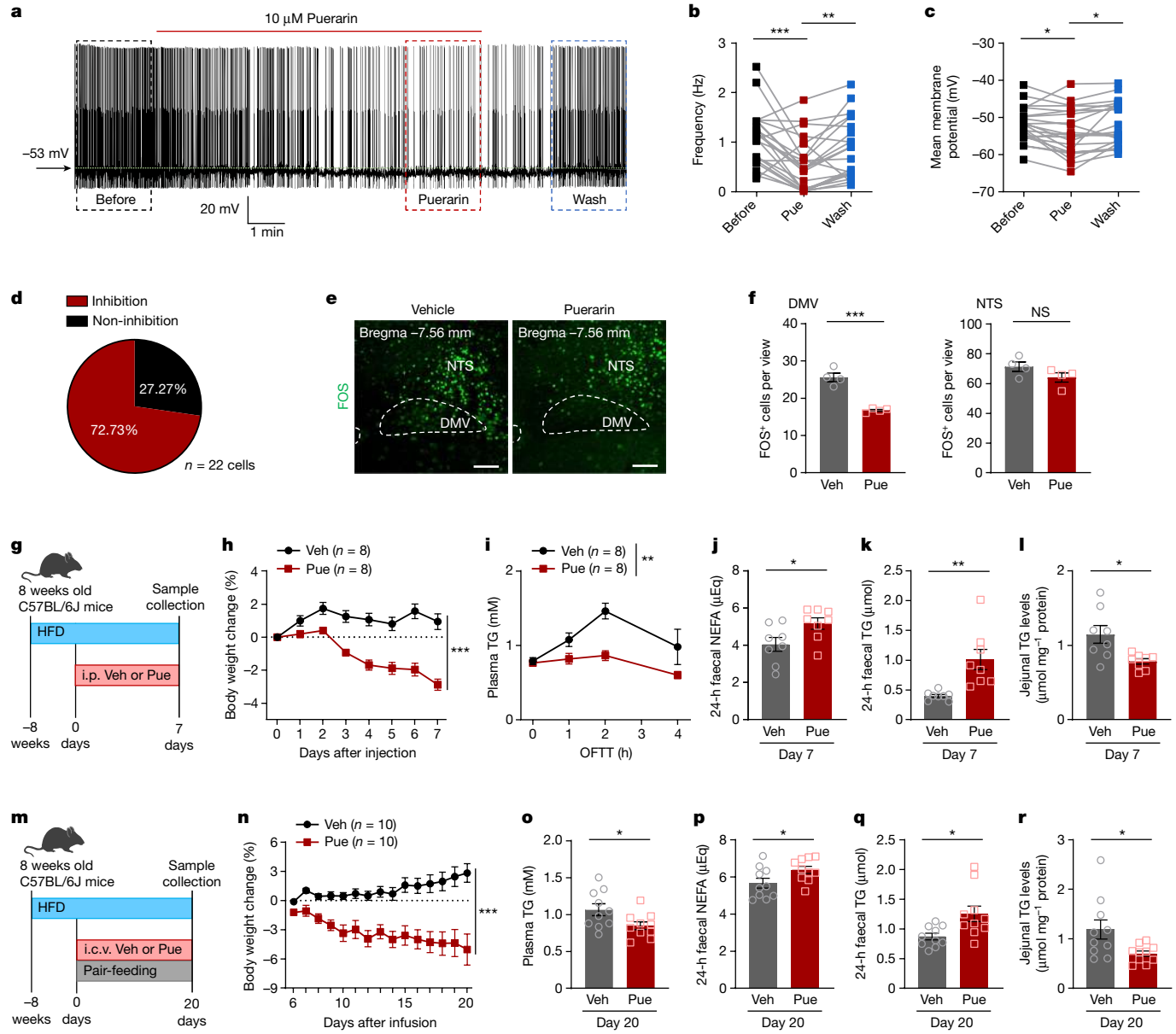

Fig. 2 | Administration of puerarin suppresses DMV activity and leads to less jejunal fat absorption. a, Representative whole-cell patch-clamp recordings from a DMV neuron before (black dashed box), during (red dashed box) and after puerarin application (blue dashed box, wash). Three periods of the recording were used for further analysis. **b**,**c**, Summary of the average action potential frequency (**b**) and mean membrane potential (**c**) from all recordings ($n = 22$). Pue, puerarin; Veh, vehicle. **d**, Percentage of DMV neurons showing puerarin-induced inhibition (red) or non-inhibition (black). **e**,**f**, Representative images (**e**) and cell count (**f**) of FOS-positive neurons in the DMV and the NTS after i.p. injection of puerarin or vehicle in pair-fed HFD mice ($n = 4$ per group). **g**, Schematic of the i.p. injection of puerarin or vehicle in mice fed a HFD. **h**–**l**, Body weight change (**h**), OFTT (**i**), faecal NEFA (**j**) and TG (**k**) content, and jejunal TG contents (**l**) ($n = 8$ per group). **m**, Schematic of the i.c.v. infusion of puerarin or vehicle in pair-fed HFD mice. **n**–**r**, Body weight change (**n**), plasma TG levels (**o**), 24-h faecal NEFA (**p**) and TG (**q**) content, and jejunal TG content (**r**) ($n = 10$ per group). Samples were collected at day 7 (**h**–**l**) and day 20 (**n**–**r**). Tissue samples were collected 2 h after 200 μl olive oil gavage (**l**,**o**,**r**). Scale bar, 100 μm (**e**). Data presented as the mean ± s.e.m. Data were analysed using two-tailed Student's *t*-test (**f**,**j**–**l**,**o**–**q**), two-tailed Mann–Whitney test (**r**), one-way ANOVA with Holm–Šídák's multiple comparisons test (**b**,**c**) or two-way ANOVA (**h**,**i**,**n**). $^*P < 0.05$, $^{**}P < 0.01$, $^{***}P < 0.001$. NS, no significance. For detailed statistics, see source data.

compared with control flox mice. Of note, when whole-cell patch-clamp recording was performed in brainstem slices, puerarin produced an inhibitory effect on most of the DMV neurons in control mice (70%, 14 out of 20 neurons), but its action was largely reduced in the absence of *Gabra1* (19.05%, 4 out of 21 neurons) (Extended Data Fig. 7f). Moreover, deletion of *Gabra1* abolished the effects of puerarin on suppressing fat absorption and body weight gain (Fig. 3i–m and Extended Data Fig. 7g). Together, our data demonstrate that puerarin exerts its inhibitory effects on the DMV–vagus axis to regulate fat absorption by binding $GABA_A$ receptors that contain the α1 subunit.

Jejunum-projecting DMV neurons in fat absorption

DMV–vagus nerves project to distinct segments of the gastrointestinal tract[32]. To target the DMV neurons that project to the jejunum, we injected a retrograde AAV virus encoding a fusion protein of wheat-germ agglutinin (WGA) and Cre recombinase (AAV-hSyn-WGA-Cre-P2A-mcherry (AAV-WGA-Cre)) into the jejunum of wild-type mice[33]. Simultaneously, a Cre-dependent hM4D(Gi) or control AAV virus was injected into the DMV region, which enabled the chemogenetic manipulation of DMV neurons projecting to the jejunum of

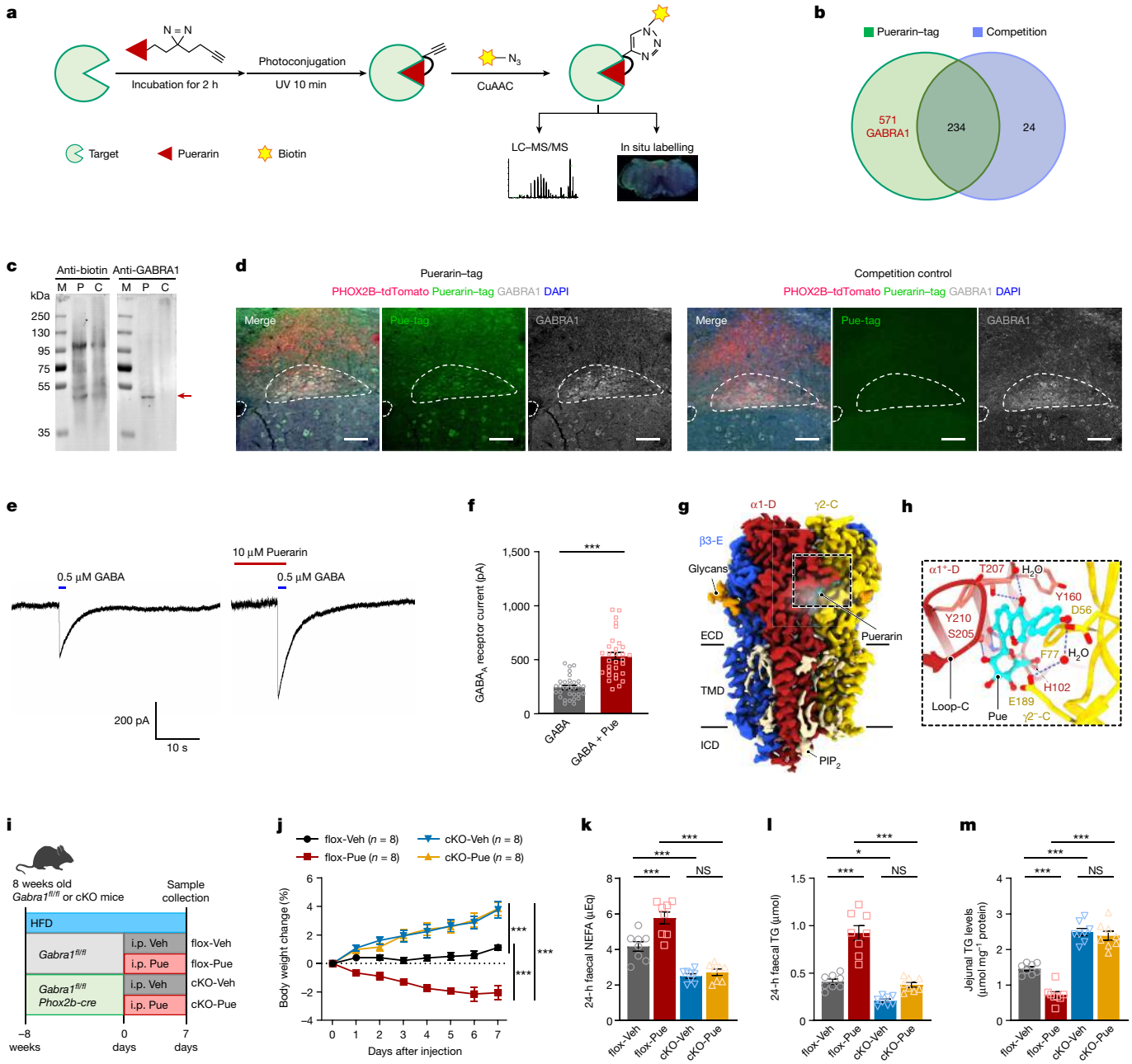

Fig. 3 | Puerarin binds to the α1 subunit of the GABA$_A$ receptor to modulate DMV neurons. a, Schematic of the photoaffinity reaction. **b**, Venn diagrams based on MS screening. After filtering the results, 571 proteins were listed to bind the puerarin-tag, including GABRA1. **c**, Western blot validation of puerarin binding to GABRA1 protein. C, competitive group; M, marker; P, puerarin-tag group. Arrow indicates GABRA1 protein. **d**, In situ labelling of the colocalization of GABRA1 and puerarin–tag in PHOX2B-expressing neurons. **e**, Representative whole-cell current traces elicited from human HEK293S cells stably expressing α1β3γ2L by a pulse of GABA alone (left) or by co-application of puerarin and GABA (right). **f**, Quantification of whole-cell current traces ($n = 31$ per group). **g**, Cryo-EM density map of the full-length human α1β3γ2L GABA$_A$ receptor in complex with puerarin. Receptor subunits are coloured red (α1), blue (β3) and yellow (γ2). Puerarin density is coloured cyan. Glycans are shown in orange and lipids in wheat. **h**, Close-up of the puerarin-binding pocket. Crucial residues that interact with puerarin are in stick representation. Blue dashed lines represent putative hydrogen bonds. **i**, Schematic of puerarin i.p. injection in *Gabra1*$^{fl/fl}$ (flox) and *Gabra1*$^{fl/fl}$ *Phox2b-cre* (cKO) mice fed a HFD. **j**, Body weight changes. **k**–**m**, 24-h faecal NEFA (**k**) and TG (**l**) content, and jejunal TG content (**m**) of flox-Veh, flox-Pue, cKO-Veh and cKO-Pue groups at day 7 ($n = 8$ per group). Tissue samples were collected 2 h after 200 μl olive oil gavage (**m**). Scale bar, 100 μm (**d**). Data presented as mean ± s.e.m. Data were analysed using two-tailed Student's *t*-test (**f**) or two-way ANOVA with Tukey's multiple comparisons test (**j**–**m**). $^*P < 0.05$, $^{**}P < 0.01$, $^{***}P < 0.001$. For detailed statistics, see source data.

WGA-hM4D(Gi) (WGA-4i) mice or control (WGA-con) mice (Fig. 4a,b). Consistent with the results observed when DMV neurons were inactivated in *Phox2b-cre* and *Chat-cre* mice, we observed that WGA-4i mice showed less body weight gain (Fig. 4c,d and Extended Data Fig. 7h), reduced plasma TG levels (Fig. 4e), increased faecal fat excretion (Fig. 4f,g) and reduced jejunal fat absorption (Fig. 4h). Using the same approach, we also inactivated DMV neurons projecting to the duodenum or ileum. No significant differences were observed in body weight, fat absorption, plasma TG levels or faecal fat excretion (Supplementary Fig. 4). These results demonstrate that DMV neurons that project to the jejunum can directly regulate fat absorption and body weight gain.

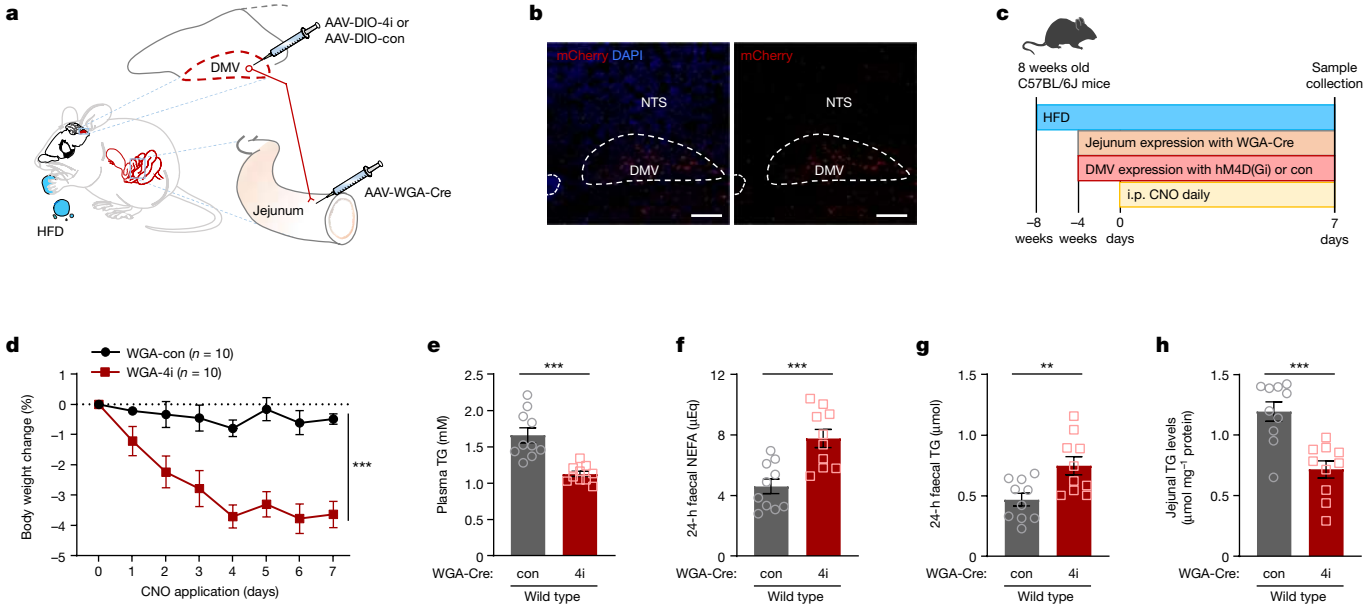

Fig. 4 | Jejunum-projecting DMV neurons control fat absorption and body weight gain. a, Abridged view of the experimental design of retrograde tracing the jejunum-projecting DMV neurons in wild-type mice fed a HFD. AAV-WGA-Cre virus was injected into the jejunum with simultaneous injection of AAV-DIO-hM4D(Gi) (WGA-4i group) or AAV-DIO-control (WGA-con group) in the DMV. **b**, Images of jejunal injection of AAV-WGA-Cre virus expressing mCherry retrogradely transported in the DMV. **c**, Schematic of chemogenetic inactivation of jejunum-projecting DMV neurons in wild-type mice fed a HFD. **d**–**h**, Changes observed after CNO application in WGA-4i and control mice ($n = 10$ per group). Body weight change over 7 days (**d**), plasma TG (**e**), 24-h faecal NEFA (**f**) and TG content (**g**), and jejunal TG content (**h**) after DMV suppression at day 7. Samples were collected 2 h after 200 μl olive oil gavage (**e**,**h**). Scale bar, 100 μm (**b**). Data presented as the mean ± s.e.m. Data were analysed using two-tailed Student's *t*-test (**f**–**h**), two-tailed Mann-Whitney test (**e**) or two-way ANOVA (**d**). $^{*}P < 0.05$, $^{**}P < 0.01$, $^{***}P < 0.001$. For detailed statistics, see source data. The mouse model in **a** was adapted from SciDraw (https://scidraw.io) under a Creative Commons licence CC BY-SA 4.0.

The DMV controls jejunal microvillus length

We next explored how puerarin and the DMV–vagal axis affect fat absorption. We first examined the expression of lipid transporters in the jejunum of DMV-inactivated mice, but did not observe significant changes (Extended Data Fig. 8a). Fat absorption efficiency is thought to strongly correlate with the change in total surface area[7]; however, there was no observable change in the length of jejunal epithelial villi after inactivation of DMV neurons or puerarin injection (Extended Data Fig. 8b–g). Of note, using EM image-based analysis, we observed that the length of jejunal microvilli lessened after inactivation of DMV neurons (Fig. 5a–c and Extended Data Fig. 8h–j). Meanwhile, the expression levels of the genes that regulate microvilli[7], including *Ezr* (which encodes ezrin), *Cdc42*, *Eps8* and *Vil1*, were significantly lower in DMV-inactivated mice than in control mice (Fig. 5d). Consistently, we found that activation of DMV neurons extended the length of jejunal microvilli and increased the expression of related genes (Extended Data Fig. 8h–k). Moreover, inactivation of the jejunum-projecting DMV neurons showed similar results, with decreased jejunal microvillus length and related gene expression (Fig. 5e–h). In line with the results of DMV inhibition, puerarin (i.p.) treatment shortened the length of microvilli and reduced the expression of related genes, whereas deletion of *Gabra1* in the DMV blunted these effects of puerarin (Fig. 5i–m and Extended Data Fig. 8l–o). Furthermore, we did not find significant changes in the duodenum or ileum after DMV inhibition or puerarin treatment (Extended Data Fig. 9). Together, these observations illustrate a model whereby the DMV–vagus pathway controls intestinal fat absorption by influencing the jejunal microvillus length (Extended Data Fig. 10).

Discussion

In physiology textbooks, dietary fat absorption is considered mainly a passive diffusion process that occurs locally in intestinal epithelial cells and can function autonomously without the control of the brain[2]. Until now, to our knowledge, brain control of fat absorption was largely unknown. In this study, we identified a brain (DMV)-to-intestinal (jejunal) pathway that controls fat absorption. We showed that inactivation of DMV neurons suppresses fat absorption in the jejunum by shortening the length of microvillus. Moreover, we demonstrated that puerarin, a natural compound used in clinical practice, can inactivate DMV neurons and suppress fat absorption through $GABA_A$ receptors, thereby revealing an applicable drug to reduce fat absorption.

The small intestine is the primary site of nutrient absorption[5]. About 160 years ago, it was observed that the small intestine of dogs could absorb fat[34]. Several studies have shown that fat absorption begins at the distal duodenum, mainly in the jejunum, substantially earlier than the absorption of carbohydrates, whereas protein cannot be completely absorbed in the small intestine and reabsorption in the large intestine is necessary as an auxiliary[18]. These observations indicated that the intestinal absorption of nutrients occurs in a region-specific manner. Here we showed that when DMV–vagus nerve activity is manipulated, changes in fat absorption mainly occurred at the jejunum. We also demonstrated that DMV neurons projecting to the jejunum directly govern the length of jejunal microvilli and fat absorption. Based on these results, our study sheds new light on how such region-specific patterns occur, which may be due to different projections of DMV–vagus nerves to distinct segments of the gastrointestinal tract[32,35]. In this study, we did not find significant alterations in oral glucose tolerance in DMV-inhibited models, which suggests that inhibition of vagal efferent nerves may not directly affect glucose absorption. We speculate that this may be because the fat absorption process does not require energy and therefore is more dependent on intestinal surface area[1]. By contrast, carbohydrate absorption largely requires the expression of ATP-dependent transporters in intestinal epithelial cells[1–3].

It has been reported that acetylcholine, a major neurotransmitter of vagus nerve terminals and enteric nerves, can increase the ratio of

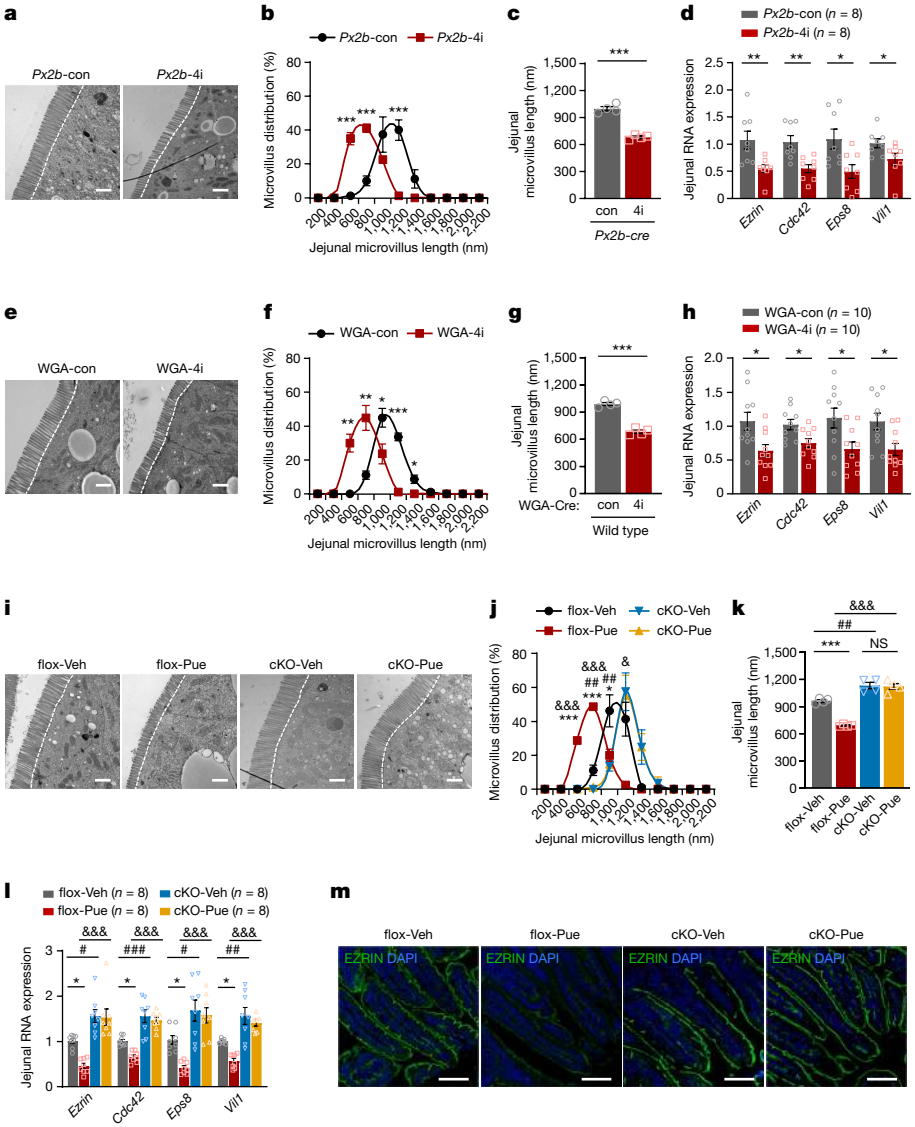

Fig. 5 | Suppression of the DMV–vagus pathway shortens jejunal microvilli to reduce fat absorption. a–**c**, Representative electron micrographs at day 7 (**a**), morphometric measurement of length distribution (**b**) and average length (**c**) of jejunal microvilli in *Px2b*-con and *Px2b*-4i mice fed a HFD. **d**, Expression of genes that regulate microvilli in the jejunum of *Px2b*-con and *Px2b*-4i mice fed a HFD. **e**–**g**, Representative electron micrographs at day 7 (**e**), morphometric measurement of length distribution (**f**) and average length (**g**) of the jejunal microvilli in WGA-con and WGA-4i mice fed a HFD. **h**, Expression of genes that regulate microvilli in the jejunum of WGA-con and WGA-4i mice fed a HFD. **i**–**k**, Representative electron micrographs at day 7 (**i**), morphometric measurement of length distribution (**j**) and average length (**k**) of the jejunal microvilli in flox-Veh, flox-Pue, cKO-Veh and cKO-Pue mice fed a HFD. **l**, Expression of genes that regulate microvilli in the jejunum of the four groups. **m**, Immunofluorescence images of EZRIN in jejunal brush-borders of the four groups at day 7. Scale bar, 1 µm (**a**,**e**,**i**) or 100 µm (**m**). For EM analyses, $n = 4$ mice per group (**b**,**c**,**f**,**g**,**j**,**k**). Data presented as mean ± s.e.m. Data were analysed using two-tailed Student's *t*-test and two-tailed Mann–Whitney test (**b**–**d**,**f**–**h**) or two-way ANOVA with Tukey's multiple comparisons test (**j**–**l**). *Comparison between *Px2b*-con and *Px2b*-4i; flox-Veh and flox-Pue; or WGA-con and WGA-4i. #Comparison between flox-Veh and cKO-Veh. &Comparison between flox-Pue and cKO-Pue. $^{*}P < 0.05$, $^{\#}P < 0.05$, $^{**}P < 0.01$, $^{\#\#}P < 0.01$, $^{***}P < 0.001$, $^{\#\#\#}P < 0.001$, $^{\&\&\&}P < 0.001$. For detailed statistics, see source data.

F-actin[36]—the core protein constituting the brush border of microvilli[7]—in smooth muscle cells. Our data revealed a significant reduction in the expression of EZRIN, which can bind to F-actin[7,37], indicating that acetylcholine might be involved in the regulation of microvillus length by the DMV–vagal axis. It is worth noting that acetylcholine can regulate the polymerization of actin filament by modulating the activity of CDC42 (ref. 36), which may be involved in the rapid change in microvillus length. Moreover, we speculate that chronic vagus suppression may lead to decreased acetylcholine levels and consequent changes in the expression of genes related to the cytoskeleton, such as those needed for Rho-GTPase signalling[7]. Thus, acetylcholine may have long-term or cumulative effects on the structure of microvilli. Further studies are needed to identify the neuromodulatory signalling involved in this brain–gut communication and its related molecular mechanism in jejunal epithelial cells.

GABAergic-mediated inactivation has an important role in controlling the neuronal activity of the DMV[26]. Among different subtypes of the $GABA_A$ receptor, *Gabra1* expression is particularly enriched in the DMV region[25]. Genetic results have illustrated that *Gabra1* is highly expressed in DMV cholinergic neurons and less abundant in GABAergic and glutamatergic neurons in the NTS[20]. Here we showed that *Gabra1* cKO resulted in increased neuronal activity in the DMV, which subsequently led to increased fat absorption. Thus, we propose that *Gabra1* plays an important part in regulating DMV activity in fat homeostasis. Presynaptic GABA release is thought to take place during NTS–DMV communication, the most relevant process in modulating vago-vagal

reflexes[38]. How the NTS senses the HFD signals from the intestine and then regulates fat absorption through NTS–DMV dialogue or the circuit formed by the vagus complex, even together with other brain regions, requires further exploration.

Of clinical significance, we showed that puerarin, an isoflavone extracted from *Radix puerariae*, inhibits the DMV–vagal pathway, which in turn reduced fat absorption. Moreover, by using cryo-EM analysis, we found that puerarin binds to GABRA1 and acts as a positive allosteric modulator. Genetic deletion of *Gabra1* in the DMV abolished the suppressive effects of puerarin on fat absorption. These observations illustrate that puerarin suppresses DMV neuronal activity and fat absorption by binding the $GABA_A$ receptor, thereby serving as a potential anti-obesity drug. Unlike orlistat, an anti-obesity drug approved by the US Food and Drug Administration, which induces loss of fat by forming a covalent bond with lipase to block lipase activity[39], puerarin reduces intestinal fat absorption by modulating DMV function and governing jejunal microvilli. Moreover, orlistat has adverse effects, including liver injury and fatty diarrhoea[40]. In this aspect, puerarin might be a safe alternative for the modulation of excess fat excretion. Therefore, future clinical studies are warranted to determine the therapeutic actions and potential side effects of puerarin in humans. In closing, our study shows that targeted control of the DMV–vagus pathway to regulate intestinal fat absorption could be a potential strategy for the treatment of obesity and metabolic diseases, paving the way for future investigations of the brain-to-gut control of nutrient absorption.

Online content

Any methods, additional references, Nature Portfolio reporting summaries, source data, extended data, supplementary information, acknowledgements, peer review information; details of author contributions and competing interests; and statements of data and code availability are available at https://doi.org/10.1038/s41586-024-07929-5.

1. Barrett, K. E., Barman, S. M., Brooks, H. L. and Yuan, J. *Ganong's Review of Medical Physiology* 26th edn. 475–476 (McGraw-Hill Medical, 2019).
2. Hall, J. E. *Guyton and Hall Textbook of Medical Physiology* 13th edn., 835–841 (Elsevier, 2016).
3. Koeppen, B. M. & Stanton, B. A. *Berne & Levy Physiology* 7th edn., 551–553 (Elsevier, 2018).
4. Alberti, K. G. M. M., Zimmet, P. & Shaw, J. The metabolic syndrome—a new worldwide definition. *Lancet* **366**, 1059–1062 (2005).
5. Mourad, F. H. & Saade, N. E. Neural regulation of intestinal nutrient absorption. *Prog. Neurobiol.* **95**, 149–162 (2011).
6. Hussain, M. M. Intestinal lipid absorption and lipoprotein formation. *Curr. Opin. Lipidol.* **25**, 200–206 (2014).
7. Delacour, D., Salomon, J., Robine, S. & Louvard, D. Plasticity of the brush border—the yin and yang of intestinal homeostasis. *Nat. Rev. Gastroenterol. Hepatol.* **13**, 161–174 (2016).
8. Chivers, D. J. & Hladik, C. M. Morphology of the gastrointestinal tract in primates: comparisons with other mammals in relation to diet. *J. Morphol.* **166**, 337–386 (1980).
9. Iqbal, J. et al. An intrinsic gut leptin–melanocortin pathway modulates intestinal microsomal triglyceride transfer protein and lipid absorption. *J. Lipid Res.* **51**, 1929–1942 (2010).
10. Travagli, R. A. & Anselmi, L. Vagal neurocircuitry and its influence on gastric motility. *Nat. Rev. Gastroenterol. Hepatol.* **13**, 389–401 (2016).
11. Browning, K. N. & Travagli, R. A. Central nervous system control of gastrointestinal motility and secretion and modulation of gastrointestinal functions. *Compr. Physiol.* **4**, 1339–1368 (2014).
12. Browning, K. N. & Carson, K. E. Central neurocircuits regulating food intake in response to gut inputs—preclinical evidence. *Nutrients* **13**, 908 (2021).
13. Doty, J. E. & Meyer, J. H. Vagotomy and antrectomy impairs canine fat absorption from solid but not liquid dietary sources. *Gastroenterology* **94**, 50–56 (1988).
14. Zhang, Z., Lam, T. N. & Zuo, Z. Radix *Puerariae*: an overview of its chemistry, pharmacology, pharmacokinetics, and clinical use. *J. Clin. Pharmacol.* **53**, 787–811 (2013).
15. Urban, D. J. & Roth, B. L. DREADDs (designer receptors exclusively activated by designer drugs): chemogenetic tools with therapeutic utility. *Annu. Rev. Pharmacol. Toxicol.* **55**, 399–417 (2015).
16. Mazzone, C. M. et al. Acute engagement of G_q-mediated signaling in the bed nucleus of the stria terminalis induces anxiety-like behavior. *Mol. Psychiatry* **23**, 143–153 (2018).
17. Gautron, L., Zechner, J. F. & Aguirre, V. Vagal innervation patterns following Roux-en-Y gastric bypass in the mouse. *Int. J. Obes.* **37**, 1603–1607 (2013).
18. Borgstrom, B., Dahlqvist, A., Lundh, G. & Sjovall, J. Studies of intestinal digestion and absorption in the human. *J. Clin. Invest.* **36**, 1521–1536 (1957).
19. Booth, C. C., Read, A. E. & Jones, E. Studies on the site of fat absorption: 1. The sites of absorption of increasing doses of I-labelled triolein in the rat. *Gut* **2**, 23–31 (1961).
20. Ludwig, M. Q. et al. A genetic map of the mouse dorsal vagal complex and its role in obesity. *Nat. Metab.* **3**, 530–545 (2021).
21. Rossi, J. et al. Melanocortin-4 receptors expressed by cholinergic neurons regulate energy balance and glucose homeostasis. *Cell Metab.* **13**, 195–204 (2011).
22. Yang, M. et al. The effect of puerarin on carotid intima-media thickness in patients with active rheumatoid arthritis: a randomized controlled trial. *Clin. Ther.* **40**, 1752–1764.e1 (2018).
23. Niphakis, M. J. & Cravatt, B. F. Enzyme inhibitor discovery by activity-based protein profiling. *Annu. Rev. Biochem.* **83**, 341–377 (2014).
24. Shieh, P., Siegrist, M. S., Cullen, A. J. & Bertozzi, C. R. Imaging bacterial peptidoglycan with near-infrared fluorogenic azide probes. *Proc. Natl Acad. Sci. USA* **111**, 5456–5461 (2014).
25. Fritschy, J. M. & Mohler, H. $GABA_A$-receptor heterogeneity in the adult rat brain: differential regional and cellular distribution of seven major subunits. *J. Comp. Neurol.* **359**, 154–194 (1995).
26. Sivarao, D. V., Krowicki, Z. K. & Hornby, P. J. Role of $GABA_A$ receptors in rat hindbrain nuclei controlling gastric motor function. *Neurogastroenterol. Motil.* **10**, 305–313 (1998).
27. Sigel, E. & Steinmann, M. E. Structure, function, and modulation of $GABA_A$ receptors. *J. Biol. Chem.* **287**, 40224–40231 (2012).
28. Laverty, D. et al. Cryo-EM structure of the human α1β3γ2 $GABA_A$ receptor in a lipid bilayer. *Nature* **565**, 516–520 (2019).
29. Masiulis, S. et al. $GABA_A$ receptor signalling mechanisms revealed by structural pharmacology. *Nature* **565**, 454–459 (2019).
30. Zhu, S. et al. Structural and dynamic mechanisms of $GABA_A$ receptor modulators with opposing activities. *Nat. Commun.* **13**, 4582 (2022).
31. Kasaragod, V. B. et al. The molecular basis of drug selectivity for α5 subunit-containing $GABA_A$ receptors. *Nat. Struct. Mol. Biol.* **30**, 1936–1946 (2023).
32. Browning, K. N., Renehan, W. E. & Travagli, R. A. Electrophysiological and morphological heterogeneity of rat dorsal vagal neurones which project to specific areas of the gastrointestinal tract. *J. Physiol.* **517**, 521–532 (1999).
33. Libbrecht, S., Van den Haute, C., Malinouskaya, L., Gijsbers, R. & Baekelandt, V. Evaluation of WGA-Cre-dependent topological transgene expression in the rodent brain. *Brain Struct. Funct.* **222**, 717–733 (2017).
34. Bernard, C. *Mémoire sur le Pancréas et sur le Role du Suc Pancréatique dans les Phénomènes Digestifs, Particulièrement dans la Digestion des Matières Grasses Neutres* (J.-B. Baillière, 1856).
35. Tao, J. et al. Highly selective brain-to-gut communication via genetically defined vagus neurons. *Neuron* **109**, 2106–2115.e4 (2021).
36. Tang, D. D. & Gunst, S. J. The small GTPase Cdc42 regulates actin polymerization and tension development during contractile stimulation of smooth muscle. *J. Biol. Chem.* **279**, 51722–51728 (2004).
37. Berryman, M., Franck, Z. & Bretscher, A. Ezrin is concentrated in the apical microvilli of a wide variety of epithelial cells whereas moesin is found primarily in endothelial cells. *J. Cell Sci.* **105**, 1025–1043 (1993).
38. Travagli, R. A., Gillis, R. A., Rossiter, C. D. & Vicini, S. Glutamate and GABA-mediated synaptic currents in neurons of the rat dorsal motor nucleus of the vagus. *Am. J. Physiol.* **260**, G531–G536 (1991).
39. Guerciolini, R. Mode of action of orlistat. *Int. J. Obes. Relat. Metab. Disord.* **21**, S12–S23 (1997).
40. Douglas, I. J., Langham, J., Bhaskaran, K., Brauer, R. & Smeeth, L. Orlistat and the risk of acute liver injury: self controlled case series study in UK Clinical Practice Research Datalink. *BMJ* **346**, f1936 (2013).

Methods

Animals

Male C57BL/6J mice were used in this study and were obtained from Shanghai Laboratory Animal. *Phox2b-cre*, *Chat-cre* and Rosa 26-CAG-loxP-STOP-loxP-tdTomato (Rosa26-tdTomato) mice were obtained from the Jackson Laboratory (stock number 016223, 006410 and 007914, respectively). *Phox2b-cre* mice and *Chat-cre* mice were crossed with Rosa26-tdTomato mice to produce PHOX2B-Cre:Rosa26-tdTomato and CHAT-Cre:Rosa26-tdTomato mice, respectively. The *Gabra1* cKO mouse model was constructed by crossing *Phox2b-cre* mice and *Gabra1*$^{fl/fl}$ mice (Cyagen Biosciences).

All animals were individually housed in a specific pathogen-free facility maintained at a temperature of 22–24 °C and a humidity of 40–70%, under a 12:12-h light–dark cycle. The mice were fed a HFD containing 60% kcal from fat (5.24 kcal g^{-1}; D12492, Research Diets) for all experiments. Eight-week-old mice were used in this study. Body weight and food intake were measured daily or according to the design of the corresponding tests. In the pair-feeding study, each mouse in a single cage was given 90% of the average daily food intake to ensure that the mice consumed all the food provided. An isoflurane inhalation anaesthesia system (R500, RWD) was used for operating on mice. All experiments complied with the guidelines of the Institutional Animal Care and Use Committee and were approved by the Institutional Animal Care and Use Committee of Shanghai Model Organisms Center.

Drug administration

The central administration experiments were performed using the i.c.v. infusion approach. Before the operation, 3.73 ng μl^{-1} puerarin (HPLC ≥ 98%; MB6183, Meilunbio) or vehicle (PBS) was injected into an Alzet capsule pump (100 μl for full filling; 1004, Durect). The capsule pump was then connected to a 2 cm polyvinyl chloride (PVC) tube for the brain infusion cannula (Brain Infusion Kit 3; 0008851, Durect). Then the entire capsule pump casing system was placed into a 37 °C saline water bath for 24 h. After the mice were anaesthetized, the capsule pump was embedded under the skin of the back close to the neck, and 2 mm of the cannula was probed into the lateral ventricle, anterior–posterior −0.7 mm, lateral 1 mm by stereotactic apparatus. The contact between the casing and skull bone was coated with glue (1496SB, 3M). After the operation, the mice were carefully returned to the cage after heat preservation at 37 °C for 1 h.

Peripheral administration experiments were conducted using daily i.p. injections, in which the dose of puerarin was 37.3 μg kg^{-1} body weight, and the dose of CNO (BML-NS105, Enzo Life Sciences) was 1.0 mg kg^{-1} body weight. Each mouse was housed in a single cage.

DREADDS

Phox2b-cre and *Chat-cre* mice were bilaterally injected with rAAV-EF1α-DIO-hM4D(Gi)-mCherry, rAAV-EF1α-DIO-hM3D(Gq)-mCherry and rAAV-EF1A-DIO-mCherry (BrainVTA) into the DMV (300 nl per side; coordinates: bregma anterior–posterior −7.1 mm, dorsal–ventral −4.5 mm, lateral ±0.2 mm) using a stereotaxic apparatus. Four weeks after rAAV injection, the mice received daily injections of CNO for 7 days. CNO-induced modulation of DMV neuronal activity was validated ex vivo (Extended Data Fig. 1).

Small intestinal injection of WGA-Cre virus

WGA-Cre mice were constructed by injecting rAAV-hSyn-WGA-Cre-P2A-mCherry (BrainVTA) into the small intestine of 8-week-old wild-type mice fed a HFD. After deep anaesthesia, the mice underwent the following surgical procedures: the hair on the abdomen was removed, the epidermis and peritoneum were opened, and the intestine (duodenum, jejunum and ileum) segments were exposed. Subsequently, 1 μl of AAV-WGA-Cre was slowly injected into the intestinal wall, with stabilization for 3 min after each injection. This process was repeated at five distinct sites in the duodenum, jejunum or ileum per mouse. The peritoneum and epidermis were then sutured. The mice were maintained with heat preservation at 37 °C for 1 h before being returned to their individual cages.

Vagotomy

After deep anaesthesia, the mice underwent the following surgical procedures: the hair on the abdomen was removed, the epidermis and peritoneum were opened, the oesophagus was isolated, and the vagus nerves on both sides of the oesophagus were exposed. A 2–3 mm segment of the vagal nerve from each side was cut off. The peritoneum and epidermis were then sutured. The mice were maintained with heat preservation at 37 °C for 1 h before being returned to their individual cages.

OFTT

After a fasting period of 4 h, each mouse was given 200 μl olive oil by oral gavage. Blood samples were collected from the orbital plexus veins after 0, 1, 2 and 4 h, and the samples were centrifuged for 10 min at 4 °C at 4,000 r.p.m. Plasma was used to assess TG levels, which were determined using a one-step enzyme method according to the manufacturer's instructions (Kehua) and were measured using microplate readers (Bio-Tek; Multiskan SKY, Thermo Fisher). Data were collected using Gen5 (v.2.09) and SkanIt RE (v.6.0.1).

Faecal and intestinal TG determination

Faecal and intestinal TG levels were determined using a commercial kit (k622-100, Biovision). In brief, 5% NP-40 was added to 10 mg of faeces or tissue along with 100 μl of lysis buffer. The homogenate was heated twice at 95 °C for 5 min each time, cooled to room temperature and then centrifuged at maximum speed (15,000 r.p.m.) for 2 min. The supernatants were collected for analysis. Supernatant (2 μl) was added to each well of the labelled plate and analysed according to the manufacturer's instructions. The 24-h faecal TG content was calculated by multiplying the sample weight by concentration, and tissue TG content was normalized by total protein levels. TG levels and total protein levels were measured using microplate readers (Bio-Tek; Multiskan SKY, Thermo Fisher) and data were collected using Gen5 (v.2.09) and SkanIt RE (v.6.0.1).

Faecal NEFA determination

Faecal NEFA was extracted using chloroform and Triton X-100 (1% Triton X-100 in pure chloroform, v/v). The samples were then air-dried at 50 °C until all the liquid evaporated, followed by vacuum drying for 30 min. Next, the samples were dissolved in 5% NP-40. Measurement was performed using a two-step enzyme method according to the manufacturer's instructions (294-63601, Wako). NEFA levels were measured using microplate readers (Bio-Tek; Multiskan SKY, Thermo Fisher), with data collected using Gen5 (v.2.09) and SkanIt RE (v.6.0.1).

Oral glucose tolerance test

After fasting overnight, each mouse was given 400 μl of a 20% glucose solution (w/v) by oral gavage. Blood samples were collected from the caudal vein at 0, 15, 30, 60 and 120 min after gavage. Blood glucose levels were measured using a blood glucose monitor (OneTouch Verio and OneTouch Ultra Vue, Johnson & Johnson).

Gastrointestinal transit and motility assessment

For total gastrointestinal transit time measurement, mice were given red carmine dye (C1022, Sigma-Aldrich), and the time from oral intake to extruding the first red pellet was recorded as the total gastrointestinal transit time. The colonic bead expulsion test was performed on mice that were fasted overnight. In brief, glass beads pretreated with

glycerin were inserted approximately 2.5 cm into the rectum of each mouse. The time required for the mice to expel the beads was recorded.

The geometric centre (GC) was measured by evaluating the intestinal location of FITC-labelled dextran (53471, Sigma-Aldrich). Mice were orally given 100 µl of a 25 mg ml^{-1} dextran solution. Thirty minutes after administration, the entire gastrointestinal tract and its content were collected and divided into 16 segments. The contents of each segment were mixed with 2 ml of 0.1 M Tris (pH 8.0) solution to obtain a supernatant containing FITC. The supernatant was then centrifuged at 500 r.p.m., and the fluorescence of the cleared supernatant was measured using a fluorescence plate reader (excitation 493 nm and emission 512–522 nm; Spark, Tecan) to quantify the fluorescent intensity in each intestinal segment. The fluorescent intensity data were collected using SparkControl (v.3.0.14.6). The GC was calculated as follows: GC = log(∑(fraction of fluorescence per segment × segment number))[41].

Haematoxylin and eosin staining

Tissue was fixed with a 4% paraformaldehyde solution overnight. Embedded tissue blocks were prepared through alcohol dehydration, xylene clearing and paraffin embedding. The paraffin sections were baked in an oven at 50 °C overnight, followed by two rounds of xylene soaking for dewaxing. The sections were then soaked in a series of graded alcohol solutions (100%, 95%, 70% and 0%), stained with haematoxylin for 5 min, rinsed and dehydrated with graded alcohol. Subsequently, the sections were stained with eosin alcohol for 1 min and dehydrated again with graded alcohol, followed by xylene clearing. Morphological analysis was performed using a microscope (Olympus), and images were captured using Olympus cellSens software (v.3.1).

Immunofluorescence analysis

Brain and intestinal tissue sections (40 µm thickness) were blocked with the serum of appropriate species, penetrated with 0.2% Triton X-100 and treated with primary antibodies (anti-FOS, 226008, Synaptic Systems; anti-GABRA1, 224205, Synaptic Systems; anti-EZRIN, 3145, Cell Signaling Technology; dilution ratio of these antibodies is 1:400). Samples were then incubated with fluorescent-conjugated secondary antibodies (goat anti-rabbit IgG, A32731, Thermo Fisher; goat anti-guinea pig IgG, PA1-28597, Thermo Fisher; both diluted 1:400). A coverslip was placed over the samples before examination under a confocal microscope (Zeiss), and images were captured using Zen (v.2.6; Zeiss). The number of positive neurons was quantified using ImageJ software (NIH).

Slice electrophysiological recording

Experiments were performed on male PHOX2B-Cre:Rosa26-tdTomato mice fed a 60% HFD for 8 weeks (aged 16–20 weeks). After anaesthesia, the brain samples were rapidly removed and immersed in ice-cold oxygenated artificial cerebrospinal fluid containing the following components: 124 mM NaCl, 3 mM KCl, 1.5 mM $CaCl_2$, 1.3 mM $MgCl_2$, 26 mM $NaHCO_3$, 1.4 mM NaH_2PO_4 and 11 mM glucose, pH at 7.2–7.4, 280–290 mOsm. Coronal brainstem slices (200–250 µm) were prepared using a vibrating microtome (VT1200S, Leica). Slices were maintained in an oxygenated bath at 33.5 °C for at least 1 h before being transferred to a recording chamber. tdTomato-positive neurons were identified under a ×40 water-immersion objective with infrared illumination, differential interference contrast optics (IR-DIC) and epifluorescence. Patch pipettes (4–6 MΩ) were pulled from borosilicate glass (Sutter Instrument) and filled with an internal solution of 125 mM potassium gluconate, 20 mM KCl, 0.05 mM EGTA, 4 mM Mg-ATP, 0.3 mM GTP, 10 mM HEPES-NaOH and 10 mM phosphocreatine, with the pH at 7.2–7.3, 285–290 mOsm. Whole-cell patch-clamp recordings were performed using an Axon 700 B amplifier. Data were filtered at 2 kHz and digitized at 10 kHz. Action potentials were examined at no inject current under current-clamp mode. Puerarin or CNO was first dissolved in PBS and diluted in artificial cerebrospinal fluid to a final concentration of 10 µM for both compounds. Recordings were analysed using pCLAMP 11 software (Molecular Devices). The average firing frequency was calculated in the last 2 min of baseline, puerarin application and washout periods shown in the figure. A cellular firing rate with over 30% change was considered a significant modulation[42] by puerarin or CNO.

Photoaffinity chemistry-based protein identification

The puerarin–tag synthesis and the photoaffinity chemistry procedures were based on previous reports[23,43,44]. In brief, puerarin (100 mg, 0.24 mmol), iodo tag (71 mg, 0.29 mmol) and K_2CO_3 (50 mg, 0.36 mmol) were dissolved in 5 ml DMF (n,N-dimethylformamide) for 24 h at room temperature. The puerarin–tag was obtained by extraction with ethyl acetate (15 ml × 3), washed with water (2 ml) and saturated salt (2 ml), followed by drying with anhydrous sodium sulfate and concentrated using column chromatography.

The brainstem samples were obtained from 16-week-old male C57BL/6J mice that had been fed a 60% HFD from 8 weeks of age. The dorsal half of the brainstem was collected, excluding the bilateral trigeminal nucleus adjacent to the dorsal vagus complex. Samples were lysed in lysis buffer containing 50 mM Tris, 150 mM NaCl, 1 mM EDTA and 1% Triton X-100. After centrifugation, the supernatant solution was collected, and puerarin–tag was added (0.25 mg puerarin–tag per 1 mg protein), 10-fold naive puerarin was added to the solution for the competitive experiment. After a 2-h reaction at room temperature, the mixture was exposed to 405 nm UV radiation on ice for 10 min. Subsequently, the equal volume of photoaffinity reaction mix (0.98 mg ml^{-1} $CuSO_4$, 2.42 mg ml^{-1} sodium ascorbate, 1.81 mg ml^{-1} Biotin-PEG3-N_3, the solvent contained 50% PBS and 50% DMSO) was added. The mixture was shaken and incubated for 10 h at room temperature (the photoaffinity reaction).

For protein solution samples, the potential target proteins were collected after passing through an avidin column (20227, Thermo Fisher), and the unbound proteins were collected by PBS wash. Proteins from the target group were identified by LC–MS and validated by western blotting.

For fixed brainstem slices, the photoaffinity reaction reflected the binding localization of puerarin in situ. After the reaction, the slices were incubated with FITC–streptavidin (SA100-02, Thermo Fisher; dilution ratio is 1:500) at 4 °C overnight, and then examined under a confocal microscope (Zeiss).

Production and purification of human α1β3γ2L $GABA_A$ receptor

The human α1β3γ2L $GABA_A$ receptor sample was produced using a stable HEK293S cell line as previously described[29,45]. In brief, cells were grown in Freestyle medium (Gibco) supplemented with 1% fetal bovine serum, L-glutamine, non-essential amino acids and selection antibiotics (250 µg ml^{-1} zeocin, 5 µg ml^{-1} blasticidin, 50 µg ml^{-1} hygromycin and 200 µg ml^{-1} geneticin), and kept in suspension by spinning at 130 r.p.m. in an 8% CO_2 environment at 37 °C. The medium was supplemented with 2 µg ml^{-1} doxycycline to induce gene expression (cell density of 2×10^6 cells per ml) along with 2.5 mM sodium butyrate and 1 µg ml^{-1} kifunensine. Cells were collected 24 h later by centrifugation (3,000*g* for 15 min) and pellets were stored at −80 °C before use.

Receptor purification was performed as previously described[28,29] from a 500 ml culture cell pellet. In summary, the cells were resuspended in a dilution buffer (50 mM HEPES pH 7.6 and 300 mM NaCl), supplemented with protease cocktail inhibitors and membranes were solubilized with 1% lauryl maltose neopentyl glycol (LMNG, Anatrace). Insoluble debris were removed by centrifugation (15,000*g* for 15 min). $GABA_A$ receptors were purified from the supernatant by affinity chromatography on a CNBr Sepharose resin (300 µl) coated with an 1D4 monoclonal antibody (University of British Columbia), followed by

on-bead reconstitution into MSP2N2 nanodiscs as follows. Beads bound with receptor were first incubated with 50 µl of phosphatidylcholine (POPC) and bovine brain extract (BBE) (85:15) for 30 min at 4 °C. POPC and BBE extract stocks (10 and 20 mg ml^{-1}, respectively) were prepared by solubilization in 3% LMNG. Beads were then allowed to settle down on ice, and excess lipids were removed. Nanodisc reconstitution was then initiated by adding 100 µl MSP2N2 (5 mg ml^{-1}) and around 50 mg biobeads (Bio-Rad). Empty nanodiscs were removed by 50 column volume dilution buffer wash. Receptors were eluted in a buffer containing 15 mM HEPES pH 7.4, 100 mM NaCl and 2.5 mM 1D4 peptide (TETSQVAPA).

Sample and grid preparation for cryo-EM analysis

Purified α1β3γ2L $GABA_A$ receptor at a concentration of 1 mg ml^{-1} was mixed with 10 µM puerarin and 200 µM GABA and incubated on ice for 30 min before grid preparation for the cryo-EM analysis. Grids were vitrified using a Leica EM GP2 plunger (Leica Microsystems). Specifically, 3.5 µl sample was applied to glow-discharged (Pelco easiGlow, 30 mA for 60 s) UltraAuFoil R1.2/1.3:300 mesh grids (Quantifoil), incubated for 30 s in a 95% chamber humidity at 14 °C, blotted for 4 s and plunged into liquid ethane cooled to −180 °C before transfer into liquid nitrogen for storage.

Data collection and processing of α1β3γ2L $GABA_A$ receptor–puerarin complex

Cryo-EM data collection was performed on a Titan Krios microscope (MRC-LMB Krios II) equipped with Falcon 4i detector and operated at 300 kV. Data collection parameters are summarized in Extended Data Table 1. Movies were motion corrected in RELION (v.4.0)[46], with its implementation of MotionCor2 (ref. 47) and contrast transfer function (CTF) was estimated using CTFFind (v.4.1.13)[48]. Particles were picked in WARP (v.1.0.9)[49], extracted in RELION and subsequently imported into Cryosparc (v.4.4.0)[50]. An ab initio map was generated from all particles followed by multiple rounds of heterogeneous refinement and single homogeneous and non-uniform refinement in Cryosparc. Particles were imported back into RELION for Bayesian polishing. A final round of non-uniform refinement was carried out in Cryosparc, resulting in a 2.4 Å resolution density map (Extended Data Fig. 6b), which was post-processed in RELION with −10 *B*-factor sharpening. Local resolution estimation was performed in RELION (Extended Data Fig. 6c).

Atomic model building and refinement

The human α1β3γ2L $GABA_A$ receptor bound to diazepam (Protein Data Bank (PDB) identifier 6HUG)[29] was used as an initial model for building and refinement. Restraints for puerarin were generated with the Grade Server (Global Phasing) online. Refinement was carried out in PHENIX (v.19.2)[51], alternating with manual inspection, rebuilding and real-space refinement in COOT[52], over multiple iterations. Model validation was performed in MolProbity[53], integrated in the PHENIX suite. Model refinement statistics are summarized in Extended Data Table 1. Receptor channel pore diameter was calculated through HOLE[54] implementation in COOT. The puerarin–α1β3γ2L $GABA_A$ receptor interface area was calculated using the PDBe PISA[55] online server. Figure panels that illustrate structural results were generated using the UCSF ChimeraX suite[56].

Western blotting

After samples were collected from the photoaffinity reaction, the loading buffer (Biocolors) was added. The proteins were separated using 10% SDS–PAGE gel electrophoresis and then transferred to a polyvinylidene fluoride membrane in an ice water bath with 20% methanol transfer solution for 2 h. The proteins were blocked with skim milk for 1 h and incubated with the primary antibody at 4 °C overnight and then with the secondary antibody at room temperature for 1 h. The Coomassie blue staining solution was BeyoBlue Coomassie Blue Super-Fast staining solution (P0017F, Beyotime). The primary antibodies used for western blotting were anti-GABRA1 (224205, Synaptic Systems; the dilution ratio is 1:1,000) and anti-BIOTIN (03-3700, Thermo Fisher; the dilution ratio is 1:1,000). The secondary antibodies (anti-mouse IgG, HRP-linked antibody, 7076, Cell Signaling Technology; rabbit anti-guinea pig HRP-linked antibody, PA1-28597, Thermo Fisher; the dilution ratio of all these antibodies is 1:1,000) were applied to develop the band with E-blot 15.1.210620.1 (E-blot).

Electrophysiological recordings from HEK293S cells

Human α1β3γ2L was expressed in a stable HEK293S cell line. Electrophysiological recordings were performed 24 h after cell subculture. The recordings were conducted using an external solution containing 140 mM NaCl, 5 mM CsCl, 2.0 mM $CaCl_2$, 1.0 mM $MgCl_2$, 10 mM glucose and 5 mM HEPES (pH 7.4 with NaOH, about 320 mOsm with sucrose). The recording pipettes were filled with intracellular solution containing 140 mM CsCl, 4 mM $MgCl_2$, 10 mM EGTA, 10 mM HEPES, 0.5 mM Na-GTP and 2 mM Mg-ATP (pH 7.2 with CsOH, about 280 mOsm). The input resistances amounted to 3–5 MΩ. GABA (0.5 µM) was used to induce membrane currents, which were recorded in the whole-cell configuration using an EPC 10 amplifier (HEKA) at 20–25 °C. Cells were held at −60 mV, and series resistance compensation of 60–80% was used and monitored during the whole-cell recording experiments. Data were acquired and analysed using PatchMaster and FitMaster software (SmartEphys HEKA). The fast-step stepper motor-driven system (RSC-160, Biologic) was used to apply GABA. Puerarin at 10 µM was applied in the medium for 5 min before adding GABA.

EM analysis

Small-intestinal tissue samples (about 1 mm^3) were fixed overnight with a polyformaldehyde–glutaraldehyde dialdehyde stationary solution. After washing twice with PBS buffer, the tissues were fixed with 1% osmium acid PBS buffer, dehydrated sequentially with 30%, 50% and 70% ethanol (10 min for each concentration), and stained with 3% uranyl acetate overnight. The tissues were then dehydrated again with ethanol, replaced with epoxy propane twice, soaked in Epon812 embedding solution and propylene oxide, dried at 60 °C for 48 h, sliced with an ultramicrotome (Leica), electron-stained with lead citrate and observed using transmission electron microscopy (Hitachi). More than 15 complete microvillus interfaces were randomly selected for imaging, and their lengths were measured using ImageJ (NIH).

RNA extraction and real-time PCR

Total RNA was extracted from the tissues using an Eastep Super Total RNA Extraction kit (LS1040, Promega) according to the manufacturer's instructions. In brief, 1 µg of RNA was reverse-transcribed to complementary DNA using PrimeScript RT master mix (RR036A, Takara). Real-time PCR was performed using a LC480 system (Roche) with SYBR Green supermix (Takara). The data were normalized to mouse *36B4*, and the results were analysed using the $2^{-\Delta\Delta Ct}$ method. All primer sets were designed to span at least one intron to avoid amplification from genomic DNA.

Statistics analysis and reproducibility

ImageJ (NIH) was used to investigate villi and microvillus length and positive cell counts. Other statistical analyses were performed using GraphPad Prism 10.2.0 (GraphPad Software). All experimental findings were repeated at least twice. Two-tailed Student's *t*-test was used for single variable comparisons with normal distribution. Mann–Whitney test (for independent samples) was used when data did not conform to normal distribution. ANOVA with Tukey's or Holm–Šídák's multiple comparisons test was used for multiple sets of measurement data comparisons. Significance was set at $P < 0.05$.

Reporting summary

Further information on research design is available in the Nature Portfolio Reporting Summary linked to this article.

Data availability

The MS data have been deposited into the ProteomeXchange Consortium through the PRIDE[57] partner repository with the dataset identifier PXD052140. Atomic coordinates and the EM density map of the α1β3γ2L $GABA_A$ receptor bound to GABA and puerarin have been deposited into the PDB and Electron Microscopy Data Bank with the accession codes 9EQG and EMD-19907, respectively. The two structures used to compare pore diameters are from previously published reports[29], with PDB accession codes 6HUP and 6HUK. Source data are provided with this paper.

41. Capasso, R. et al. Fatty acid amide hydrolase controls mouse intestinal motility in vivo. *Gastroenterology* **129**, 941–951 (2005).
42. Toda, C. et al. UCP2 regulates mitochondrial fission and ventromedial nucleus control of glucose responsiveness. *Cell* **164**, 872–883 (2016).
43. Jackson, P. & Lapinsky, D. J. Appendage and scaffold diverse fully functionalized small-molecule probes via a minimalist terminal alkyne-aliphatic diazirine isocyanide. *J. Org. Chem.* **83**, 11245–11253 (2018).
44. Gao, J., Mfuh, A., Amako, Y. & Woo, C. M. Small molecule interactome mapping by photoaffinity labeling reveals binding site hotspots for the NSAIDs. *J. Am. Chem. Soc.* **140**, 4259–4268 (2018).
45. Dostalova, Z. et al. Human α1β3γ2L γ-aminobutyric acid type A receptors: high-level production and purification in a functional state. *Protein Sci.* **23**, 157–166 (2014).
46. Kimanius, D., Dong, L., Sharov, G., Nakane, T. & Scheres, S. H. W. New tools for automated cryo-EM single-particle analysis in RELION-4.0. *Biochem. J.* **478**, 4169–4185 (2021).
47. Zheng, S. Q. et al. MotionCor2: anisotropic correction of beam-induced motion for improved cryo-electron microscopy. *Nat. Methods* **14**, 331–332 (2017).
48. Rohou, A. & Grigorieff, N. CTFFIND4: fast and accurate defocus estimation from electron micrographs. *J. Struct. Biol.* **192**, 216–221 (2015).
49. Tegunov, D. & Cramer, P. Real-time cryo-electron microscopy data preprocessing with Warp. *Nat. Methods* **16**, 1146–1152 (2019).
50. Punjani, A., Rubinstein, J. L., Fleet, D. J. & Brubaker, M. A. cryoSPARC: algorithms for rapid unsupervised cryo-EM structure determination. *Nat. Methods* **14**, 290–296 (2017).
51. Liebschner, D. et al. Macromolecular structure determination using X-rays, neutrons and electrons: recent developments in Phenix. *Acta Crystallogr. D Struct. Biol.* **75**, 861–877 (2019).
52. Casanal, A., Lohkamp, B. & Emsley, P. Current developments in Coot for macromolecular model building of electron cryo-microscopy and crystallographic data. *Protein Sci.* **29**, 1069–1078 (2020).
53. Chen, V. B. et al. MolProbity: all-atom structure validation for macromolecular crystallography. *Acta Crystallogr. D Biol. Crystallogr.* **66**, 12–21 (2010).
54. Smart, O. S., Neduvelil, J. G., Wang, X., Wallace, B. A. & Sansom, M. S. HOLE: a program for the analysis of the pore dimensions of ion channel structural models. *J. Mol. Graph.* **14**, 354–360, 376 (1996).
55. Krissinel, E. & Henrick, K. Inference of macromolecular assemblies from crystalline state. *J. Mol. Biol.* **372**, 774–797 (2007).
56. Pettersen, E. F. et al. UCSF ChimeraX: structure visualization for researchers, educators, and developers. *Protein Sci.* **30**, 70–82 (2021).
57. Perez-Riverol, Y. et al. The PRIDE database resources in 2022: a hub for mass spectrometry-based proteomics evidences. *Nucleic Acids Res.* **50**, D543–D552 (2022).

Acknowledgements We thank C.-C. Hui, Y. A. Zeng, W. Shen, J. Hu, C. Zhan and X. R. Ma for their suggestions on this study; G. Shu for the gift of Rosa26-tdTomato mice and N. Xu for *Chat-cre* mice; Y. Chen for confocal technical support; R. Piskorowski for providing puerarin for cryo-EM analysis; J. Grimmett, T. Darling and I. Clayson for scientific computing support; S. Chen, G. Cannone, G. Sharov, A. Yeates and B. Ahsan for EM support; staff at the Core Facility of Basic Medical Sciences, SJTUSM for EM technical support; and A. R. Aricescu for providing manuscript comments, materials and access to cryo-EM infrastructure. This work was supported by grants from the National Natural Science Foundation of China (82088102 and 91957124), the National Key Research and Development Program of China (2022YFC2505201 and 2021YFA1301103), the National Natural Science Foundation of China (92157204, 82250901, 81930021, 91857205 and 82100905), the Innovative research team of high-level local universities in Shanghai, Shanghai Municipal Education Commission (2023ZKZD22), the Science and Technology Commission of Shanghai Municipality (21JC1404400), and the Shanghai Sailing Program (21YF1440700), NATCM's Project of High-level Construction of Key TCM Disciplines (ZYYZDXK-2023070). The cryo-EM work was funded by an EMBO long-term fellowship (ALTF137-2019), a Marie Sklodowska Curie individual fellowship (GABAARComp-897707) and the UK Medical Research Council (MC_UP_1201/15).

Author contributions J.W. and W.W. designed the experiments and supervised the study. Q. Lyu, W.X., Q.M. and M.Y. performed the animal and molecular experiments. Y.C., M.Y., Y.Y. and C.S. performed the microinjection experiments. Q. Li., A.N., S.J., P.G. and W.R. performed the whole-cell patch-clamp recording experiments. C.Y. and F.N. performed the puerarin-tag synthesis. S.S., Q. Lyu, B.Z., X.Y. and Z.R. performed the preliminary cryo-EM experiments. V.B.K. produced the final α1β3γ2L $GABA_A$ receptor sample and solved its GABA and puerarin-bound structure by cryo-EM. Y.B. and G.N. contributed to discussions. Q. Lyu, W.X., C.Z., R.L. and J.W. wrote the manuscript. J.W., R.L., G.N. and C.Z. edited the manuscript.

Competing interests The authors declare no competing interests.

Additional information
Supplementary information The online version contains supplementary material available at https://doi.org/10.1038/s41586-024-07929-5.

Correspondence and requests for materials should be addressed to Jiqiu Wang or Weiqing Wang.

Peer review information *Nature* thanks A. Radu Aricescu and the other, anonymous, reviewer(s) for their contribution to the peer review of this work.

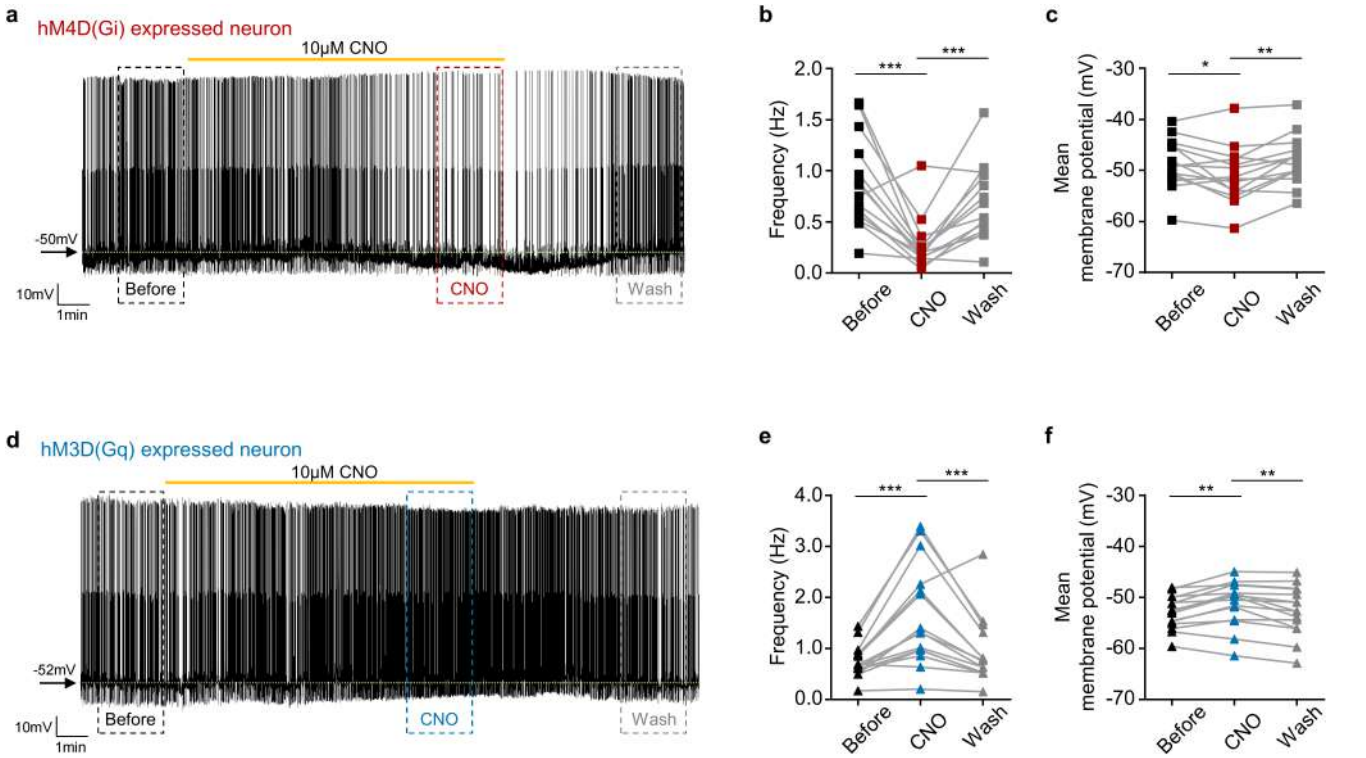

Extended Data Fig. 1 | Chemogenetic inactivation or activation of DMV neurons ex vivo. a-c, Representative whole cell patch-clamp recordings from a DMV neuron expressing the hM4D(Gi), before (black dashed box), during (red dashed box) and after CNO application (grey dashed box, wash) (**a**). Summary of average action potential (AP) frequency (**b**), and mean membrane potential (**c**) of a total of 14 neurons. **d-f**, Representative whole cell patch-clamp recordings from a DMV neuron expressing the hM3D(Gq), before (black dashed box), during (blue dashed box) and after CNO application (grey dashed box, wash) (**d**). Summary of average AP frequency (**e**), and mean membrane potential (**f**) of a total of 15 neurons. Data were analyzed using paired one-way ANOVA with Holm-Šídák's multiple comparisons test. Data are presented as mean ± S.E.M. * $P < 0.05$; ** $P < 0.01$; *** $P < 0.001$; NS, no significance. Detailed statistics see source data.

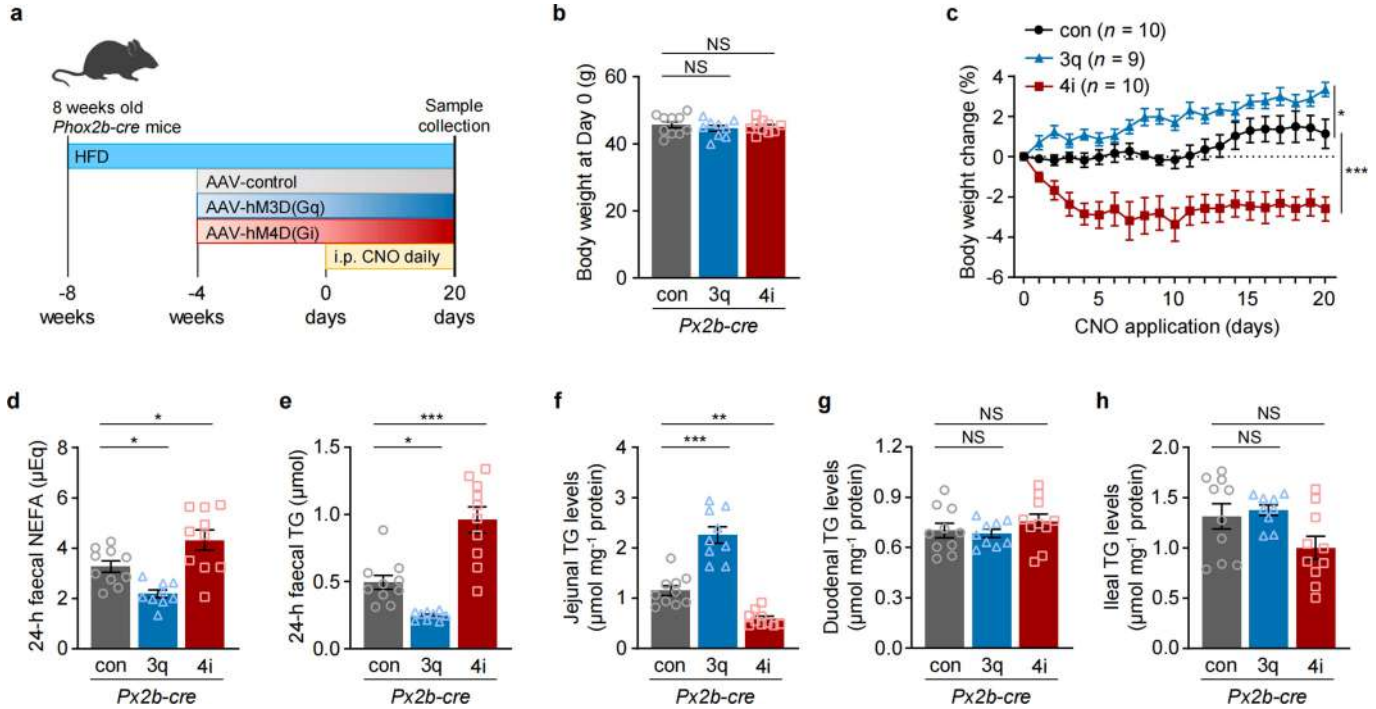

Extended Data Fig. 2 | The activation of DMV neurons promote jejunal fat absorption and increases body weight gain in HFD mice. a, Schematic of chemogenetic activation and inactivation of DMV neurons in mice fed on HFD. **b**-**h**, CNO-induced vagal neuronal manipulation in DMV by DREADDS system in activation (3q, $n = 9$), suppression (4i, $n = 10$) and control (con, $n = 10$) mice. Body weight before CNO application (**b**) and body weight change (**c**) during 20 days, 24 h fecal NEFA (**d**) and TG contents (**e**), jejunal (**f**), duodenal (**g**) and ileal (**h**) TG contents at day 20. Samples were collected 2 h after 200 μL olive oil gavage (**f** to **h**). Data were analyzed using two-way ANOVA (**c**) and one-way ANOVA with Holm-Šídák's multiple comparisons test (**b**, **d** to **h**). Data are presented as mean ± S.E.M. ns, no significance; * $P < 0.05$; ** $P < 0.01$; *** $P < 0.001$. Detailed statistics see source data.

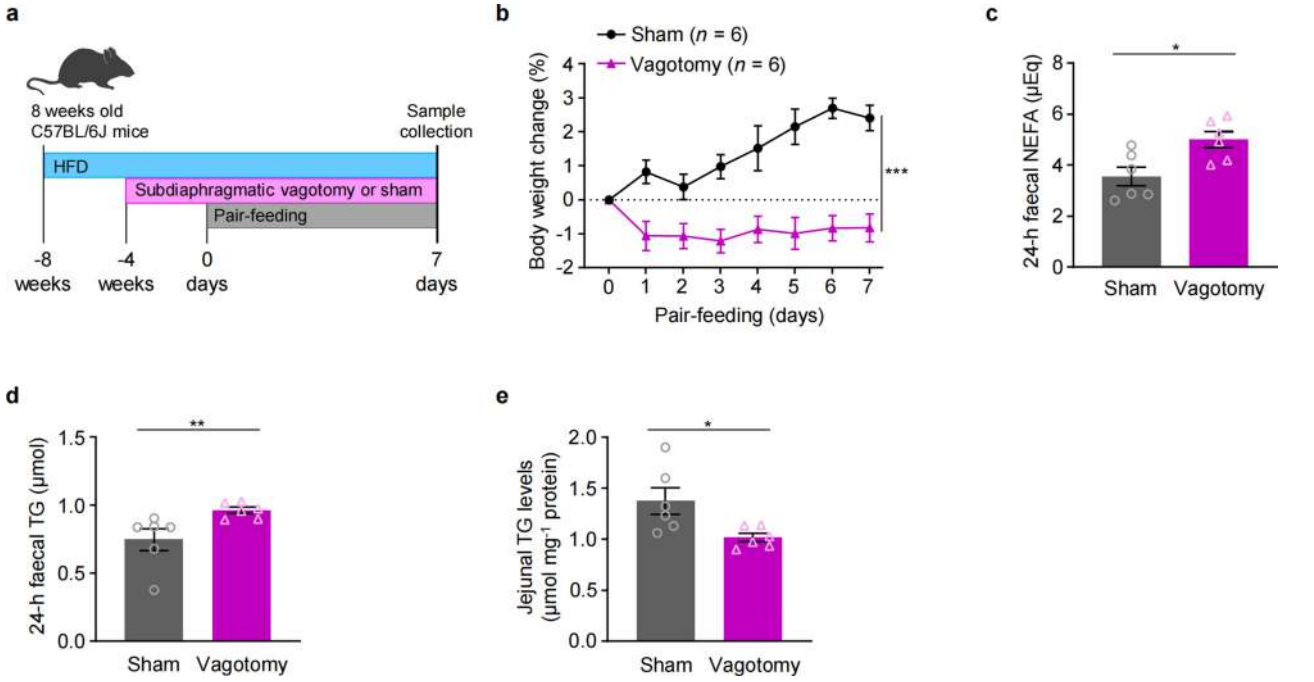

Extended Data Fig. 3 | Subdiaphragmatic vagotomy suppresses jejunal fat absorption. a, Schematic of the subdiaphragmatic vagotomy and sham mice fed on HFD ($n = 6$ per group). **b**, Body weight change of two groups. **c**, 24 h fecal NEFA contents. **d**, 24 h fecal TG contents. **e**, Jejunal TG contents of two groups with tissue collection 2 h after 200 μL olive oil gavage. Data were analyzed using two-way ANOVA (**b**), two-tailed Student's *t* test (**c** and **e**) and two-tailed Mann-Whitney test (**d**). Data are presented as mean ± S.E.M. * $P < 0.05$, ** $P < 0.01$, *** $P < 0.001$. Detailed statistics see source data.

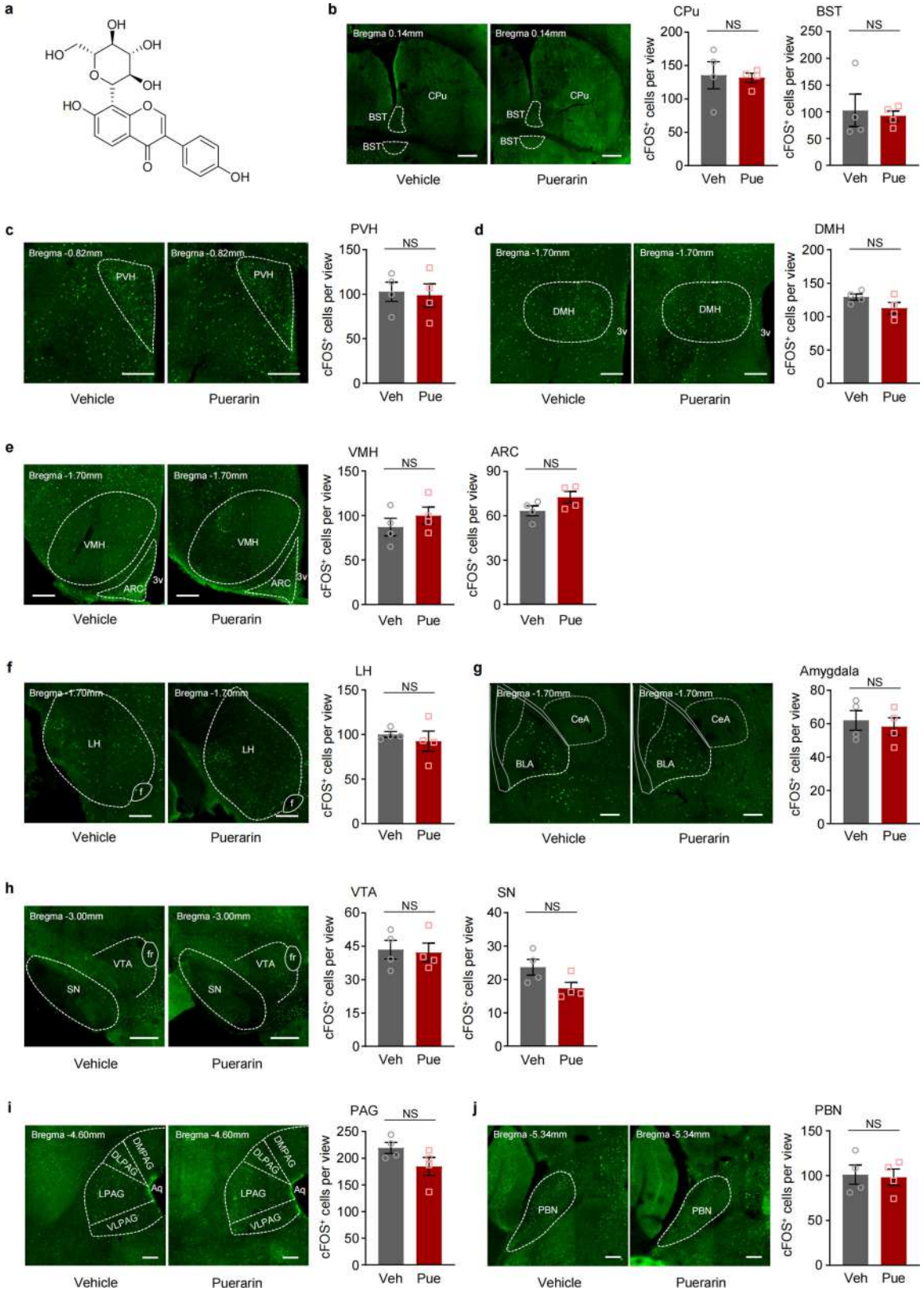

Extended Data Fig. 4 | Neuronal activation in different brain regions after puerarin administration. a, Chemical structure of puerarin molecule. **b**-**j**, cFOS immunostaining of brain regions in mice treated with i.p. injection of puerarin and vehicle under pair-feeding HFD, and counts of c-fos positive neurons in various rostral-caudal nucleus ($n = 4$ per group), including striatum (CPu) and bed nucleus of stria terminalis (BST) (**b**), paraventricular hypothalamus (PVH) (**c**), dorsomedial hypothalamus (DMH) (**d**), ventromedial hypothalamus (VMH) and arcuate nucleus of hypothalamus (ARC) (**e**), lateral hypothalamus (LH) (**f**), basolateral and central amygdaloid nucleus (BLA and CeA, Amygdala) (**g**), ventral tegmental area (VTA) and substantia nigra (SN) (**h**), dorsomedial, dorsolateral, lateral and ventrolateral periaqueductal gray (PAG including DMPAG, DLPAG, LPAG, and VLPAG) (**i**), and parabrachial nucleus (PBN) (**j**). Scale bar, 500 μm (**b**, **h**), 200 μm (**d**-**g**, **i**-**j**) and 100 μm (**c**). Data were analyzed using two-tailed Student's *t* test and are presented as mean ± S.E.M. Veh, vehicle; Pue, puerarin. ns, no significance. Detailed statistics see source data.

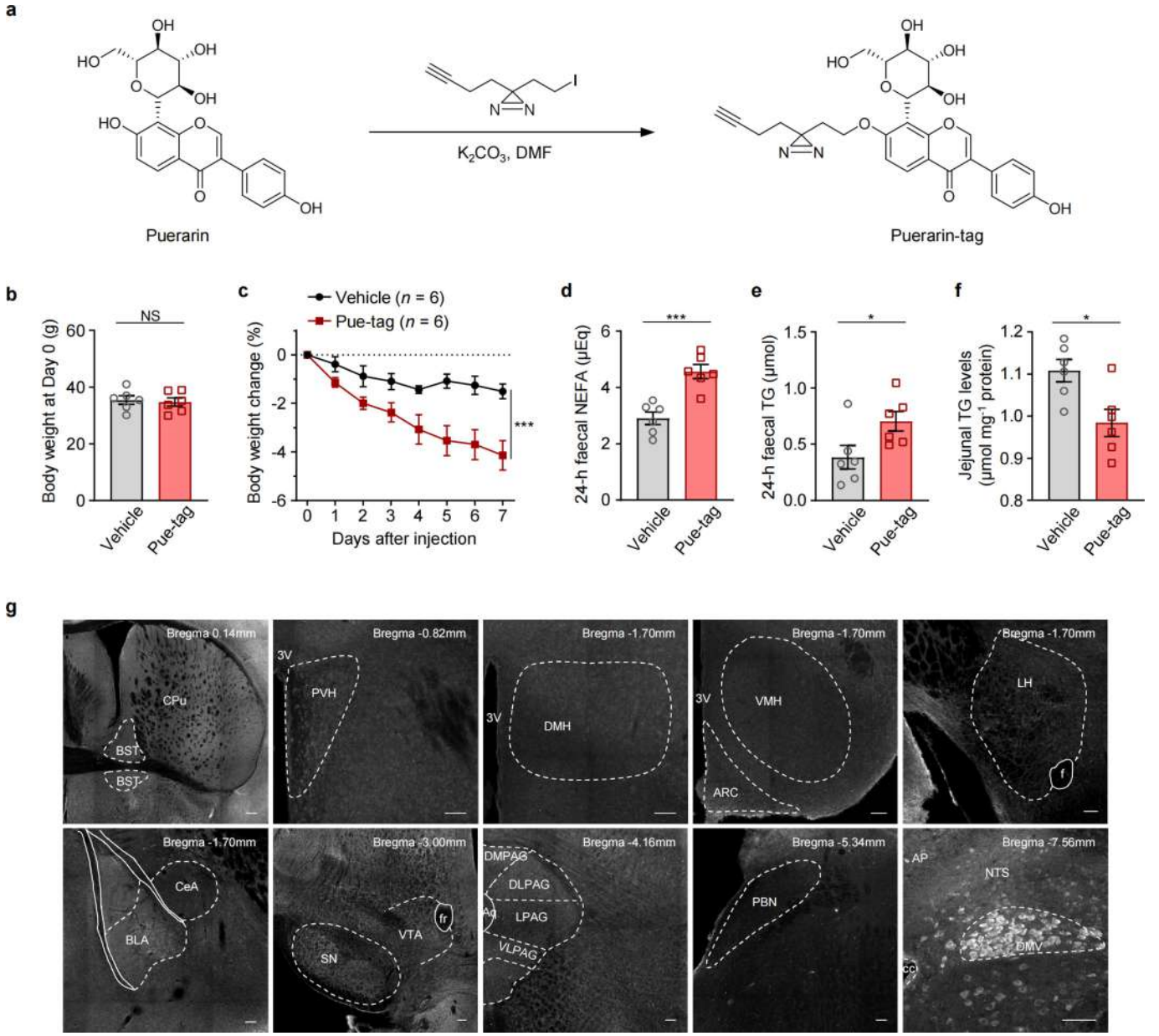

Extended Data Fig. 5 | The preparation and functional validation of puerarin-tag probe. a, Simplified chemical reaction of puerarin-tag synthesis. **b**-**f**, Body weight before injection (**b**), body weight change (**c**), 24 h fecal NEFA (**d**) and TG (**e**) contents, and jejunal TG contents (**f**) in mice treated with puerarin-tag and vehicle i.p. injection, respectively ($n = 6$ per group). **g**, Representative images of GABRA1 immunostaining in striatum (CPu), bed nucleus of stria terminalis (BST), paraventricular hypothalamus (PVH), dorsomedial hypothalamus (DMH), ventromedial hypothalamus (VMH), arcuate nucleus of hypothalamus (ARC), lateral hypothalamus (LH), basolateral and central amygdaloid nucleus (BLA and CeA, Amygdala), ventral tegmental area (VTA), substantia nigra (SN), dorsomedial, dorsolateral, lateral and ventrolateral periaqueductal gray (PAG, including DMPAG, DLPAG, LPAG, and VLPAG), parabrachial nucleus (PBN), nucleus of solitary tract (NTS), area postrema (AP), and dorsal motor nucleus of vagus (DMV). Scale bar, 100 μm. Data were analyzed using two-way ANOVA (**c**) and two-tailed Student's *t* test (**b**, **d** to **f**). Data are presented as mean ± S.E.M. Veh, vehicle; Pue, puerarin. $^{*}P < 0.05$, $^{**}P < 0.01$, $^{***}P < 0.001$. Detailed statistics see source data.

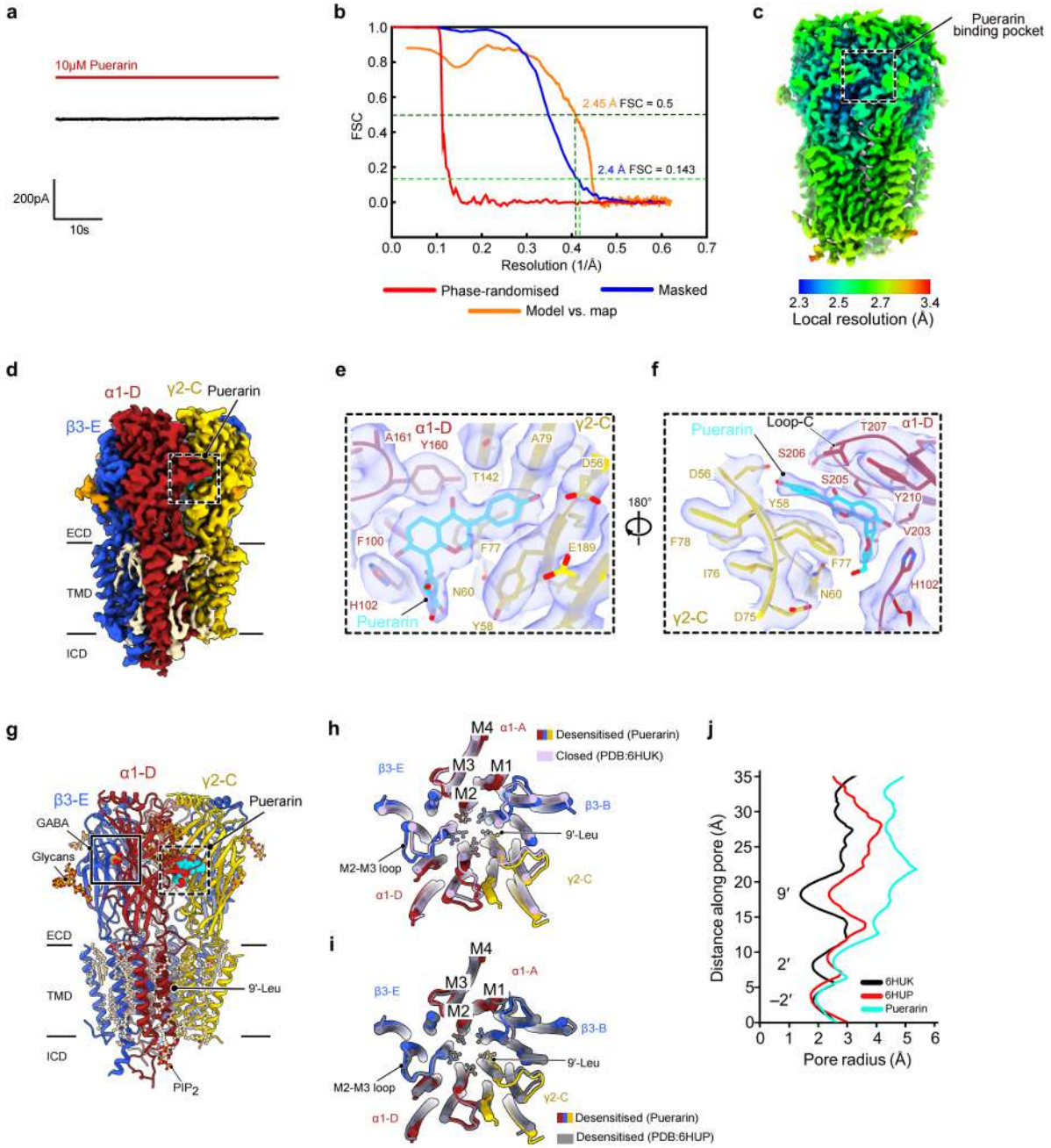

Extended Data Fig. 6 | Single particle cryo-EM reconstruction of the α1β3γ2L GABA$_A$ receptor bound to puerarin. a, Representative whole-cell current traces elicited from human α1β3γ2L stably expressed HEK293S cell line by puerarin alone. **b**, Fourier shell correlation (FSC) curves of the cryo-EM density map reconstruction (phase-randomized in red, masked in blue) and model vs. map correlation (orange) of the α1β3γ2L GABA$_A$ receptor bound to puerarin. **c**, The final unsharpened map coloured according to the local resolution estimated by RELION. **d**, Cryo-EM density map of the GABA$_A$ receptor-puerarin complex. The receptor subunits are coloured in red (α1), blue (β3) and yellow (γ2). The puerarin density, observed only at the $\alpha1^+/\gamma2^-$ interface, is coloured in cyan. The dashed rectangle marks the puerarin binding pocket. **e**-**f**, Enlarged views of the binding pocket where the density map is semi-transparent (light blue), the protein main chains are in cartoon representation, puerarin and the neighbouring side chains are in stick representation. **g**, Cartoon representation of the GABA$_A$ receptor bound to puerarin. Lipids surrounding the transmembrane region are in the ball and stick representation, while GABA and puerarin are shown as spheres. **h**-**i**, Top view cartoon representations of the puerarin-bound GABA$_A$ receptor transmembrane domain (TMD, coloured according to panel **g**) superimposed with structures of the bicuculline-bound α1β3γ2L (**h**, PDB:6HUK) and diazepam-bound α1β3γ2L (**i**, PDB:6HUP). The side chains of the 9′-activation gate leucine residues are shown in ball and stick representation. **j**, Channel pore radii profiles of the GABA$_A$ receptor bound to puerarin (cyan), bicuculline (black, PDB:6HUK) and diazepam (red, PDB:6HUP).

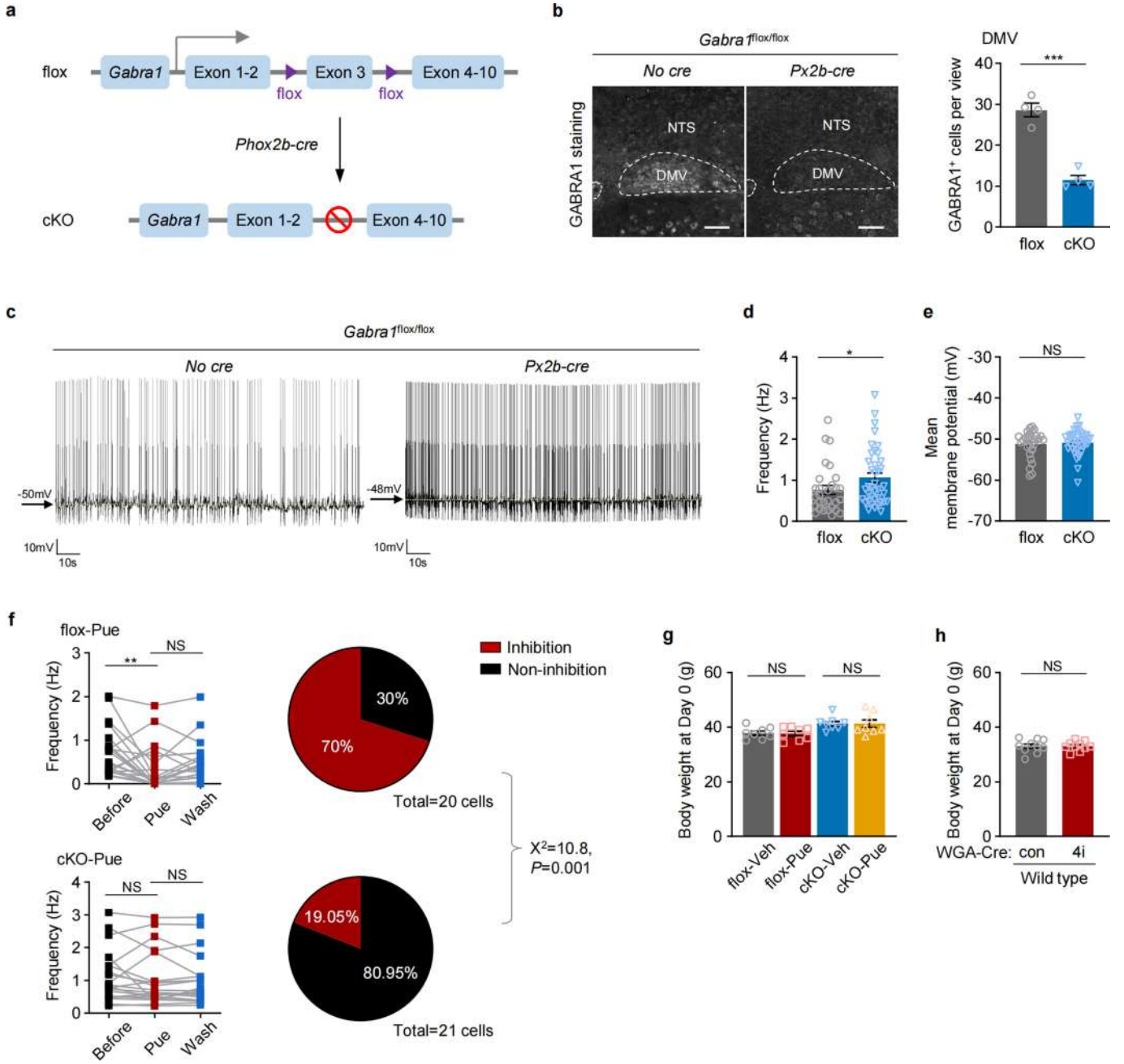

Extended Data Fig. 7 | Puerarin could not exert inhibitory effects on DMV neurons in *Gabra1* cKO mice. a, Construction strategy of *Gabra1* vagal conditional knockout mice. **b**, Representative GABRA1 fluorescent staining and quantification in DMV of cKO and flox control mice ($n = 4$ per group). **c**, Representative whole cell patch-clamp recordings from a DMV neuron of control mouse (left), and a DMV neuron from cKO mouse (right). **d**-**e**, Average AP frequency (**d**), and mean membrane potential (**e**) of recorded DMV neurons from flox ($n = 29$) and cKO mice ($n = 39$). **f**, AP frequency and percentage of DMV neurons from flox ($n = 20$) and cKO ($n = 21$) mice showing puerarin-associated inhibition or non-inhibition. **g**, The body weight of flox and cKO mice before puerarin and vehicle injection ($n = 8$ per group). **h**, The body weight of WGA-con and WGA-4i before CNO application ($n = 10$ per group). Scale bar, 100 μm (**b**). Data were analyzed using two-tailed Student's *t* test (**b** and **h**) and two-tailed Mann-Whitney test (**d** to **e**), two-sided Chi-square test (**f**), one-way ANOVA with Holm-Šídák's multiple comparisons test (**f**) and two-way ANOVA with Tukey's multiple comparisons test (**g**). Data are presented as mean ± S.E.M. * $P < 0.05$; ** $P < 0.01$; *** $P < 0.001$. Detailed statistics see source data.

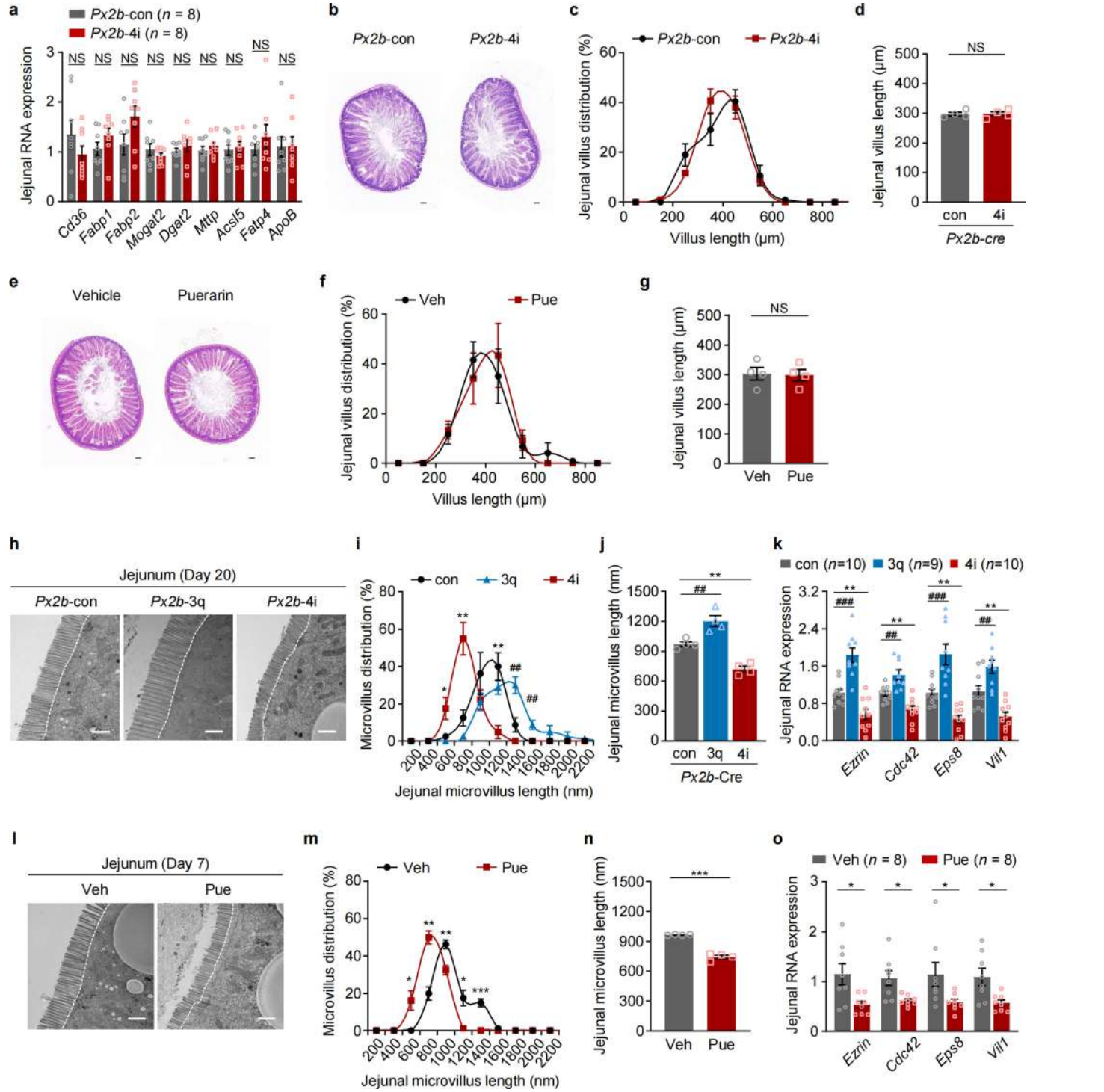

Extended Data Fig. 8 | The gene expression and morphological changes in jejunum regulated by DMV-vagus axis manipulation or puerarin treatment. **a**, The expression of genes related to jejunal lipid transporters in *Px2b*-4i and *Px2b*-con mice. **b**-**d**, HE staining of the jejunum (**b**), morphometric measurement of length distribution (**c**) and average length of jejunal villi (**d**) in *Px2b*-4i and *Px2b*-con mice (n = 4/group). **e**-**g**, HE staining of the jejunum (**e**), morphometric measurement of length distribution (**f**) and average length of jejunal villi (**g**) in puerarin- and vehicle-injected mice ($n = 4$ per group). **h**-**j**, Representative electron micrographs (**h**), morphometric measurement of length distribution (**i**) and average microvillus length (**j**) in the jejunum of 3q, 4i and con mice ($n = 4$ per group). **k**, The expression of genes related to microvillus length in jejunum of the three groups. **l**-**n**, Representative electron micrographs (**l**), morphometric measurement of length distribution (**m**) and average microvillus length (**n**) in the jejunum of puerarin- and vehicle-treated mice ($n = 4$ per group). **o**, The expression of genes related to microvillus length in jejunum of the two groups. Scale bar, 100 μm for optical micrographs; 1 μm for electron micrographs. Data were analyzed using two-tailed Student's *t* test and two-tailed Mann-Whitney test (**a** to **g**, and **m** to **o**) and one-way ANOVA with Holm-Šídák's multiple comparisons test (**i** to **k**). Data are presented as mean ± S.E.M. Veh, vehicle; Pue, puerarin; *Px2b*, *Phox2b*. * indicates *Px2b*-con vs. *Px2b*-4i or Veh vs. Pue or con vs. 4i, # Indicates con vs. 3q. *, $^{\#}P < 0.05$; **, $^{\#\#}P < 0.01$; ***, $^{\#\#\#}P < 0.001$. Detailed statistics see source data.

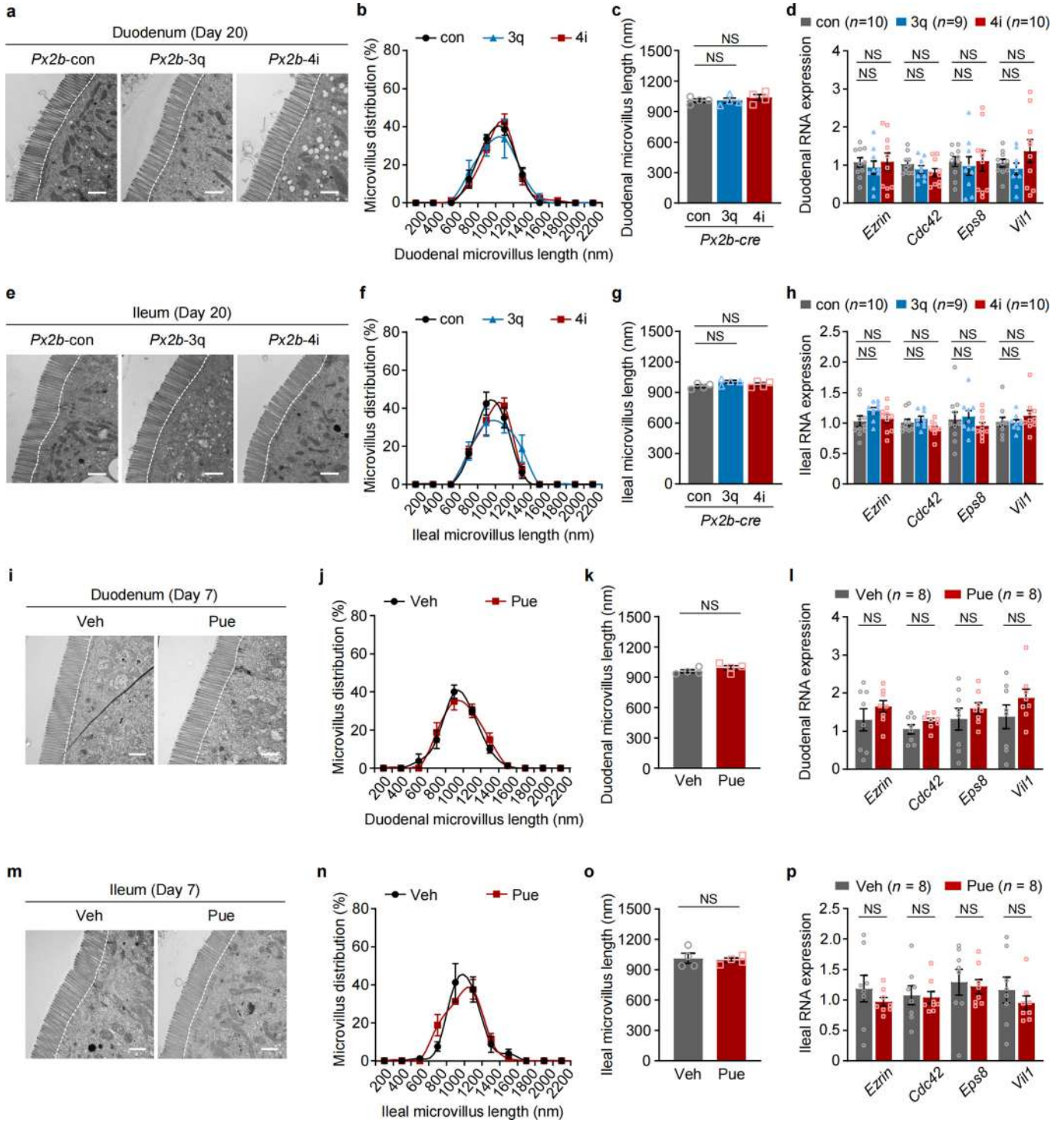

Extended Data Fig. 9 | The gene expression and morphology of duodenum and ileum regulated by DMV-vagus axis manipulation or Puerarin treatment. **a**-**d**, Representative electron micrographs (**a**), morphometric measurement of length distribution (**b**), average microvillus length (**c**) and related gene expression (**d**) in the duodenum of 3q, 4i and con mice. **e**-**h**, Representative electron micrographs (**e**), morphometric measurement of length distribution (**f**), average microvillus length (**g**), and related gene expression (**h**) in the ileum of the three groups. **i**-**l**, Representative electron micrographs (**i**), morphometric measurement of length distribution (**j**), average microvillus length (**k**) and related gene expression (**l**) in the duodenum of Puerarin- and vehicle-injected mice. **m**-**p**, Representative electron micrographs (**m**), morphometric measurement of length distribution (**n**), average microvillus length (**o**) and related gene expression (**p**) in the ileum of the two groups. Scale bar, 1 μm for electron micrographs. For electron microscopy analysis, $n = 4$ mice in each group (**b**, **c**, **f**, **g**, **j**, **k**, **n** and **o**). Data were analyzed using one-way ANOVA with Holm-Šídák's multiple comparisons test (**a** to **h**), two-tailed Student's *t* test and two-tailed Mann-Whitney test (**i** to **p**). Data are presented as mean ± S.E.M. Veh, vehicle; Pue, puerarin; *Px2b*, *Phox2b*. Detailed statistics see source data source data.

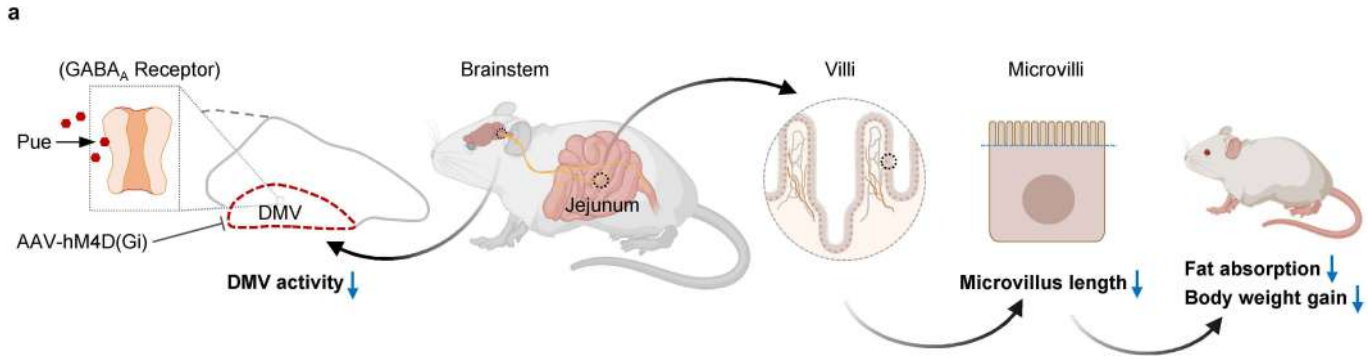

Extended Data Fig. 10 | Summary of DMV regulating jejunal fat absorption through a brain-to-gut axis. a, Schematic of a brain-to-gut axis controlling fat absorption in the jejunum, in which inhibition of DMV by chemogenetics or Puerarin leads to microvilli shortening, fat absorption suppression and consequently weight loss. (Figure was created with BioRender).

Extended Data Table 1 | Cryo-EM data collection, atomic model refinement and validation statistics

	α1β3γ2L $GABA_AR$-puerarin complex (EMDB:**19907**) (PDB: **9EQG**)
Data collection and processing	
Microscope	MRC LMB Krios II
Magnification	96000
Voltage (kV)	300
Detector	Falcon 4i
Electron exposure ($e^-/Å^2$)	40
Defocus range (μm)	-1.0 to -2.2
Pixel size (Å)	0.824
Flux on the detector (e^-/pix/sec)	6.48
Symmetry imposed	C1
Number of collected movies	8747
Initial particle images (no.)	1,932,720
Final particle images (no.)	122,065
Map resolution (Å)	2.4
FSC threshold (0.143)	
Map resolution range (Å)	2.3-6
Refinement	
Initial model used (PDB code)	6HUP
Model resolution (Å)	2.45
FSC threshold (0.5)	
Map sharpening *B* factor ($Å^2$)	-10
Model composition	
Non-hydrogen atoms	15464
Protein residues	1726
Waters	258
Glycan atoms	442
GABA atoms	14
Lipid atoms	442
Ions	3
Puerarin atoms	30
B factors ($Å^2$)	
Protein	72.6
Waters	67.4
Glycans	90.1
GABA	59.1
Lipids	85.6
Ions	78.2
Puerarin	69.3
R.m.s. deviations	
Bond lengths (Å)	0.003
Bond angles (°)	0.703
Validation	
MolProbity score	0.94
Clashscore	1.79
Poor rotamers (%)	0.0
Ramachandran plot	
Favored (%)	98.1
Allowed (%)	1.9
Disallowed (%)	0.0

nature portfolio

Corresponding author(s): Jiqiu Wang, Weiqing Wang

Last updated by author(s): Jul 15, 2024

Reporting Summary

Nature Portfolio wishes to improve the reproducibility of the work that we publish. This form provides structure for consistency and transparency in reporting. For further information on Nature Portfolio policies, see our Editorial Policies and the Editorial Policy Checklist.

Statistics

For all statistical analyses, confirm that the following items are present in the figure legend, table legend, main text, or Methods section.

n/a	Confirmed	
☐	☒	The exact sample size (*n*) for each experimental group/condition, given as a discrete number and unit of measurement
☐	☒	A statement on whether measurements were taken from distinct samples or whether the same sample was measured repeatedly
☐	☒	The statistical test(s) used AND whether they are one- or two-sided *Only common tests should be described solely by name; describe more complex techniques in the Methods section.*
☐	☒	A description of all covariates tested
☐	☒	A description of any assumptions or corrections, such as tests of normality and adjustment for multiple comparisons
☐	☒	A full description of the statistical parameters including central tendency (e.g. means) or other basic estimates (e.g. regression coefficient) AND variation (e.g. standard deviation) or associated estimates of uncertainty (e.g. confidence intervals)
☐	☒	For null hypothesis testing, the test statistic (e.g. *F*, *t*, *r*) with confidence intervals, effect sizes, degrees of freedom and *P* value noted *Give P values as exact values whenever suitable.*
☒	☐	For Bayesian analysis, information on the choice of priors and Markov chain Monte Carlo settings
☒	☐	For hierarchical and complex designs, identification of the appropriate level for tests and full reporting of outcomes
☒	☐	Estimates of effect sizes (e.g. Cohen's *d*, Pearson's *r*), indicating how they were calculated

Our web collection on statistics for biologists contains articles on many of the points above.

Software and code

Policy information about availability of computer code

Data collection	Triglyceride and non-esterified fatty acid levels were collected by Gen5 2.09 and SkanIt RE 6.0.1. The fluorescent intensity of geometric center test was collected by SparkControl_V3.0.14.6. Hematoxylin-eosin (HE) staining images were captured by Olympus cellSens (Ver3.1). The fluorescent images were taken by Zen 2.6 (Zeiss). Slice electrophysiological recordings were analyzed by pCLAMP 11 software (Molecular Devices). Electrophysiological recordings from HEK293S cell line were analyzed by FitMaster software RELION (ver 4.0), CTFFind (ver 4.1.13), WARP (ver 1.0.9), Cryosparc (ver 4.4.0), PHENIX (ver 19.2), MolProbity, ChimeraX, and COOT were used to collect cryo-EM images, build, refine the model, channel pore diameter and interface area calculation. Eblot 15.1.210620.1 was used to collect western blot images.
Data analysis	Villus and microvillus length, positive cell counts were investigated by imageJ (1.48v). Statistical analyses were performed using Graphpad Prism 10.2.0. Receptor channel pore diameter was calculated through HOLE implementation in COOT. Puerarin-GABAA receptor interface area was calculated through PDBe PISA online server.

For manuscripts utilizing custom algorithms or software that are central to the research but not yet described in published literature, software must be made available to editors and reviewers. We strongly encourage code deposition in a community repository (e.g. GitHub). See the Nature Portfolio guidelines for submitting code & software for further information.

Data

Policy information about availability of data

All manuscripts must include a data availability statement. This statement should provide the following information, where applicable:

- Accession codes, unique identifiers, or web links for publicly available datasets
- A description of any restrictions on data availability
- For clinical datasets or third party data, please ensure that the statement adheres to our policy

The mass spectrometry data have been deposited to the ProteomeXchange Consortium via the PRIDE partner repository with the dataset identifier PXD052140. Atomic coordinates and the EM density map of the a1b3g2L GABAA receptor bound to GABA+Puerarin have been deposited in the Protein Data Bank (PDB) and Electron Microscopy Data Bank (EMDB) with the accession codes 9EQG and EMD-19907, respectively. The two structures used to compare pore diameters are from previously published reports, the PDB accession codes are 6HUP and 6HUK.

Research involving human participants, their data, or biological material

Policy information about studies with human participants or human data. See also policy information about sex, gender (identity/presentation), and sexual orientation and race, ethnicity and racism.

Reporting on sex and gender	N/A
Reporting on race, ethnicity, or other socially relevant groupings	N/A
Population characteristics	N/A
Recruitment	N/A
Ethics oversight	N/A

Note that full information on the approval of the study protocol must also be provided in the manuscript.

Field-specific reporting

Please select the one below that is the best fit for your research. If you are not sure, read the appropriate sections before making your selection.

☒ Life sciences ☐ Behavioural & social sciences ☐ Ecological, evolutionary & environmental sciences

For a reference copy of the document with all sections, see nature.com/documents/nr-reporting-summary-flat.pdf

Life sciences study design

All studies must disclose on these points even when the disclosure is negative.

Sample size	Sample size was determined based on similar studies in this field: n=6-10 mice were used to determine the bodyweight, metabolic functions and gene expressions (ref. 9, 21); n=4 mice were used to determine the quantification of the immunofluorescence images and EM images (PMID: 27912057; PMID: 26638070); more than 10 cells in each group were used to determine the electrophysiological recording (ref. 32).
Data exclusions	Exclusion criteria is pre-established before the experiments. If done usually due to samples that deemed to be outliers or animals in abnormal condition.
Replication	All experimental findings were repeated at least twice.
Randomization	Samples of western blotting needed to be loaded in a specific order to generate the final figures; the transgenic mice was allocated into experimental groups according to their genotype. Otherwise, randomization was applied wherever possible. For example, the samples were proceeded and subjected to mass spectrometer and biochemical analysis (such as TG and NEFA)in random orders; mice of the same genotype was allocated randomly into experimental groups.
Blinding	Blinding was applied wherever possible. For example, in the immunofluorescence imaging experiments, mass spectrometry experiments, and electrophysiological experiments of the chemogenetic model and GABRA1 cKO model, the investigators were blinded to the treatment groups. During the treatment of live animals, cages were labeled with code names during sample collection and processing, and these code names were later revealed by the individuals who picked and treated the animals. Otherwise, for the remaining studies, the individual researchers were aware of the study design, and blinding was not performed during data collection and analysis.

Reporting for specific materials, systems and methods

We require information from authors about some types of materials, experimental systems and methods used in many studies. Here, indicate whether each material, system or method listed is relevant to your study. If you are not sure if a list item applies to your research, read the appropriate section before selecting a response.

Materials & experimental systems

n/a	Involved in the study
☐	☒ Antibodies
☐	☒ Eukaryotic cell lines
☒	☐ Palaeontology and archaeology
☐	☒ Animals and other organisms
☒	☐ Clinical data
☒	☐ Dual use research of concern
☒	☐ Plants

Methods

n/a	Involved in the study
☒	☐ ChIP-seq
☒	☐ Flow cytometry
☒	☐ MRI-based neuroimaging

Antibodies

Antibodies used

1. anti-c-fos, catalog No. 226008, Synaptic Systems, Germany (1:400)
2. anti-GABRA1, catalog No. 224205, Synaptic Systems, Germany(1:400 for IHC, 1:1000 for WB)
3. anti-Biotin, catalog No. 03-3700, Thermofisher, USA (1:1000)
4. anti-Ezrin, catalog No. 3145, Cell Signaling Technology, USA (1:400)
5. Streptavidin, (FITC), catalog No. SA100-02 , Thermofisher, USA (1:500)
6. Rabbit anti-Guinea Pig HRP-linked Antibody, catalog No. PA1-28597, Thermofisher, USA (1:1000)
7. Anti-mouse IgG, HRP-linked Antibody, catalog No. 7076, Cell Signalling Technology, USA (1:1000)
8. Goat anti-Guinea Pig IgG (H+L) Highly Cross-Adsorbed Secondary Antibody, Alexa Fluor 647, catalog No. PA1-28597, Thermofisher, USA (1:400)
9. Goat anti-Rabbit IgG (H+L) Highly Cross-Adsorbed Secondary Antibody, Alexa Fluor Plus 488, catalog No. A32731, Thermofisher, USA (1:400)

Validation

Validation data about the antibodies purchased from commercial vendors are available on the manufacturer's website. Rabbit monoclonal c-fos antibody (catalog No. 226008) was validated by manufacturer: https://www.sysy.com/product/226008. Guinea pig polyclonal GABRA1 antibody (catalog No. 224205) was validated by manufacturer: https://www.sysy.com/product/224205#list. Mouse monoclonal Biotin antibody (catalog No. 03-3700) was validated by manufacturer: https://www.thermofisher.cn/cn/zh/antibody/product/Biotin-Antibody-clone-Z021-Monoclonal/03-3700. Rabbit Ezrin Antibody (catalog No. 3145) was validated by manufacturer: https://www.cellsignal.cn/products/primary-antibodies/ezrin-antibody/3145.

Eukaryotic cell lines

Policy information about cell lines and Sex and Gender in Research

Cell line source(s)

The HEK293S cell line (based on ATCC CRL-3022) expressing the alpha1beta3gamma2L GABAA receptor has been previously described (PMID 24288268).

Authentication

Authentication was not performed for this study.

Mycoplasma contamination

Cells have been routinely tested for mycoplasma and they are negative.

Commonly misidentified lines
(See ICLAC register)

No commonly misidentified cell lines were used.

Animals and other research organisms

Policy information about studies involving animals; ARRIVE guidelines recommended for reporting animal research, and Sex and Gender in Research

Laboratory animals

Male C57BL/6J mice used in this study were obtained from Shanghai Laboratory Animal Co. Ltd. Phox2b-Cre, Chat-Cre, and Rosa26-CAG-loxP-STOP-loxP-tdTomato (Rosa26-tdTomato) mice were obtained from the Jackson Laboratory (Stock No. 016223, 006410, and 007914; Bar Harbor, USA). Phox2b-Cre mice and Chat-Cre mice were crossed with Rosa26-tdTomato mice to produce Phox2b-Cre:Rosa26-tdTomato and Chat-Cre:Rosa26-tdTomato mice. Gabra1 conditional knockout mouse model was constructed using Phox2b-Cre mice and Gabra1 flox/flox mice (Cyagen Biosciences (Suzhou) Inc).
All animals were individually housed in a specific pathogen-free facility maintained at a temperature of 22-24°C and a humidity of 40%-70%, under a 12:12-hour light-dark cycle. The mice were fed a high-fat diet (HFD) containing 60% kcal from fat (5.24 kcal/g; catalog No. D12492, Research Diets Inc., USA) for all experiments. The mice used were 8 weeks old. Body weight and food intake were measured daily or according to the design of the corresponding tests. In the pair-feeding study, to ensure that mice consumed all the food provided, each mouse in a single cage was given 90% of the average daily food intake. To reduce fasting time, half of the food was provided in the morning and the other half in the evening.

Wild animals

The study did not involve wild animals.

Reporting on sex	Adult male mice were used in our experiments. In this study, we find vagal nerves regulating fat absorption to control body weight in mice on high fat diet. Under high fat diet condition, male mice were prone to gain more weight than female mice [PMID: 36198723 & PMID: 35953023]. Thus, we used male mice in this paper. Further studies are needed to investigate whether vagal nerves can also regulate fat absorption in jejunum and control bodyweight in female mice.
Field-collected samples	The study did not involve samples collected from the field.
Ethics oversight	All experiments were performed in compliance with the guidelines of the Institutional Animal Care and Use Committee (IACUC) and were approved by the Institutional Animal Care and Use Committee of Shanghai Model Organisms Center, China.

Note that full information on the approval of the study protocol must also be provided in the manuscript.

Plants

Seed stocks	N/A
Novel plant genotypes	N/A
Authentication	N/A